École polytechnique de Louvain

Cubsats's study in formation for Earth observation

Author: **Eliott HUBIN**
Supervisors: **Cristophe CRAEYE, Jan THOEMEL**
Readers: **Dimitri LEDERER, Maxime DROUGUET**
Academic year 2022–2023
Master [120] in Mechanical Engineering

Abstract

This thesis delves into the complex world of Earth observation by leveraging Cubesats as compact satellite platforms. The research explores the application of Global Navigation Satellite Systems-Reflectometry (GNSS-R) to address an ambitious project: the replacement of large conventional continuous aperture antennas with non-regular arrays of individual elements mounted on Cubesats. These miniaturized satellites are then deployed in coordinated formation flights in orbit to create functioning antenna arrays. This innovative approach aims to address cost and development challenges while maintaining high-resolution Earth observation capabilities. In pursuit of this goal, the study explores the complex challenges imposed by orbital mechanics and electromagnetic constraints. The study reveals the inability to maintain a fixed formation over time and parallel to the Earth's surface. As a result, the need for solutions for the extraction of data with consistent resolution is a necessity. The results of the investigation highlight promising spiral configurations that successfully manage orbital dynamics while meeting strict electromagnetic criteria in terms of resolution and sidelobe heights. Through these findings, the study contributes to advancing our understanding of utilizing Cubesats in formation for Earth observation.

Acknowledgment

I would like to begin by expressing my heartfelt gratitude to Professor Christophe Craeye for his unfailing availability and guidance throughout this project. His contagious passion, insightful advice, and dedicated support have been instrumental in bringing this work to fruition. I am also deeply grateful for his valuable input during the rigorous review of my thesis.

A warm thank you goes to Dr. Jan Thoemel, without whom the mechanical aspect of this project would not have materialized. His consistent encouragement has been a driving force that motivated me to excel and stay committed throughout this entire project.

I also extend my gratitude to the members of my jury, Professor Dimitri Lederer and Ir. Maxime Drouguet for their time and expertise invested in evaluating my work.

Lastly, I would like to express my deepest appreciation to my family, friends, and loved ones who have provided unfailing support both mentally and physically. Their constant presence and steadfast support have accompanied me on this journey from one home to another, from one country to another, as I worked on bringing this thesis to fruition.

List of Acronyms

- **GNSS**: Global Navigation Satellite Systems
- **GNSS-R**: Global Navigation Satellite Systems-Reflectometry
- **CW equations**: Clohessy-Wiltshire equations
- **ECI**: Earth-centered inertial
- $\mathcal{H}$**-frame**: Hill frame
- $\mathcal{I}$**-frame**: Inertial frame

Contents

Introduction

The development of Earth observation satellites has made a lasting impact on the progress of space exploration, providing invaluable data and insights into our planet's climate, environment, and resources. The journey of Earth observation started in 1978 with the launch of the first major passive microwave satellite [5]. This marked the inception of remote sensing from space, setting the stage for continuous advancements. In recent times, a revolutionary approach has emerged, harnessing signals of opportunity, exemplified by the Global Navigation Satellite Systems-Reflectometry (GNSS-R). Its ability to provide global coverage, all-weather monitoring, real-time data, and cost-effectiveness has propelled it beyond traditional observation methods, overcoming their limitations and introducing a new era of Earth monitoring. This innovative bi-static radar allowed the use of passive antenna receivers and opened up possibilities for more compact satellite designs.

However, challenges persisted. Traditional GNSS-R techniques still demanded large aperture antennas, which consequently required satellites of considerable size. This interdependency between antenna dimensions and satellite scale presented both financial and mechanical complexities. From this point, a groundbreaking solution has emerged: the replacement of conventional continuous aperture antennas with non-regular arrays comprising independent elements. This innovative change relies on miniaturized satellites, commonly known as Cubesats, operating in formation, each equipped with one element. While the notion of employing a network of antennas collaboratively isn't novel and is extensively employed on Earth, its adaptation within the realm of space exploration remains an emerging and evolving concept.

This thesis concentrates on the exploration of formations of Cubesats, striving to mimic the behavior of continuous aperture antennas. Moreover, this ambitious endeavor inherently presents a multitude of technical challenges to overcome. On one hand, the implementation of this type of technology requires addressing numerous concerns related to orbital mechanics. These include the risks associated with potential collisions among satellites within a formation and the fact that satellites operating on slightly elliptical orbits can cause variations in their relative flight configurations over time. These factors significantly impact the integrity of the analysis conducted for Earth observation. On the other hand, once these mechanical challenges are mastered, electromagnetic requirements come into play. It is true that cost constraints inevitably limit the number of Cubesats available to replicate a continuous-aperture behaviour. Consequently, achieving an optimal arrangement of satellites to establish an effective antenna array becomes of primary importance. This optimal positioning is crucial for attaining a sufficiently high ground resolution to effectively extract data during Earth observation.

Given the challenges associated with the establishment of Cubesats' formations in orbit, several questions arise: What orbital constraints do the laws of physics impose, and how can we manage them? How does this interplay of constraints affect ground resolution during Earth observation? How does the positioning of satellites within an antenna array shape the observation beam directed towards the Earth? And amidst these considerations, which configuration emerges as the most promising for future applications?

To answer these questions, this thesis unfolds as follows. The first chapter (1) introduces the concepts of GNSS-R and Cubesat technology, explaining the diverse mechanical and electromagnetic constraints and criteria that must be considered throughout the course of this project. Chapter 2 delves into interpreting the Clohessy-Wiltshire equations, which govern the relative motion of multiple objects in space. Chapter 3 focuses on the dynamic orbital aspect of the project, starting by determining acceptable relative flight configurations based on the laws of physics. This is followed by a development to position these flight configurations in an absolute geocentric reference frame. The calculation of the specular point is also addressed. Chapter 4 shifts the focus to the electromagnetic aspect of the project, aiming to develop tools for comparing various types of Cubesat formations. A preliminary analysis based on array factors is conducted in this chapter, with the goal of highlighting the most promising configurations. Chapter 5 concludes this work by conducting a more in-depth analysis of the promising configurations emerging from Chapter 4. This analysis aims to investigate how the mechanical constraints encountered impact the ground signal illumination.

By addressing this innovative method of space-based Earth monitoring, this thesis seeks to contribute to the advancement of Cubesats technologies and their significant role in high-resolution Earth observation. Thus, the insights gained from this research will serve as preliminary steps for future applications of Cubesats' formations.

Chapter 1

Description of the Problem

This section aims to describe the problem of utilizing formation-flying Cubesats to enhance ground resolution. It focuses on the GNSS-R technology and the development of miniaturized satellites. Additionally, it discusses the constraints related to orbital mechanics and electromagnetic criteria that need to be considered for the successful implementation of the mission.

1.1 Observation method: GNSS-R

GNSS, or Global Navigation Satellite System, is a global network of satellites that provides positioning, navigation, and timing services to users on Earth [13]. While it exists numerous GNSS systems in operation worldwide, this thesis focuses on the European Union's GNSS called Galileo [35].

One critical aspect of GNSS is the utilization of different frequency bands for signal transmission. Specifically, the Galileo satellites employ the L1 frequency band, which operates at 1,575.42 MHz [11]. This implies a wavelength close to $\lambda = 0.2$ m.

Within the field of GNSS, an innovative technique stands out, the GNSS-R, or Global Navigation Satellite System Reflectometry. This method utilizes the signals emitted by GNSS satellites and their reflections from the Earth's surface to gather valuable geophysical information [30]. The key concept of GNSS-R involves adopting a bi-static radar configuration, where separate objects serve as signal transmitters and receivers, unlike traditional mono-static radar systems, where both transmission and reception occur on the same device. To be more specific, in the particular case of the Galileo system, the GNSS will be positioned within the Medium Earth Orbit (MEO), at an altitude of 23 222 km [12]. However, the receiver will be located in Low Earth Orbit (LEO), positioned below 2000 km of altitude.

In summary, the signal will be transmitted from a GNSS transmitter system, then reflected on the Earth's surface at a point commonly known as the specular point, and finally intercepted by the receiver. However, while the term *specular point* is commonly used to describe the location on the Earth's surface where the reflection of the signal occurs, it is essential to recognize that in the context of GNSS-R, this point is theoretical. Instead, the topography influences the scattering and the spatial resolution resulting in a *glistening zone*. This represents the area where significant reflections of GNSS signals from the Earth's surface are captured within the receiver's field of view, influenced by the distribution of surface slopes [38].

Finally, upon receiving and analyzing the reflected GNSS signals, the receiver can extract valuable information regarding surface roughness, soil moisture, vegetation density, sea surface height, and others. The GNSS-R approach offers numerous advantages, including cost-effectiveness, global coverage, and the ability to operate in all weather conditions. As a result, it becomes a powerful tool for Earth observation and environmental monitoring.

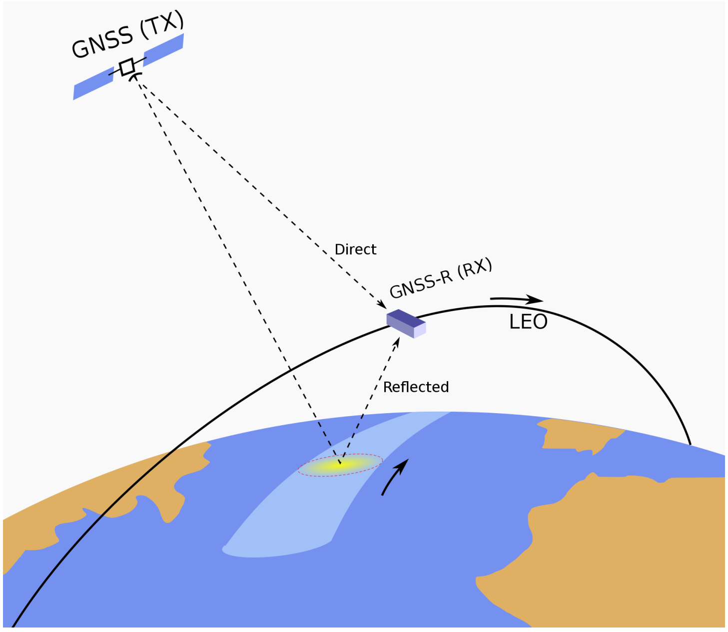

Figure 1.1: Illustration of the GNSS-R principle

1.2 Cubesats

Cubesats have emerged as a small revolution in the field of space technology, unlocking new frontiers in innovation and space exploration. These miniature satellites, with an average size of only 10 cm^3, standardized in size and shape, have opened up unprecedented opportunities, particularly for Earth observation missions. The advantages of Cubesats extend beyond cost reduction in launching and development; they facilitate deployment, can be launched as auxiliary payloads, and allow the formation of swarms [23].

Indeed, several Cubesats can be deployed in a formation, forming a robust satellite constellation. If each of these satellites carries identical antennas, the constellation transforms into what is known as an antenna array. Such a mobile antenna network can be deployed to observe the Earth with exceptional resolution. Achieving a similar result with a single antenna would have required a larger, more expensive, and less easily deployable option than the Cubesats [26].

In the specific case of this study, Cubesats are employed as receivers of navigation signals transmitted by GNSS satellites. These Cubesats are designed to operate at an altitude of 400 kilometers within the L1 frequency range, used by Galileo satellites. By taking advantage of the reflections of these GNSS signals from various surfaces, such as land, water, ice, and vegetation, these miniaturized satellites can passively collect geophysical information without the need for independent signal generation.

This passive sensing approach is particularly well-suited for Cubesats due to their compact size, which limits their capacity to independently generate electromagnetic signals. Implementing independent signal generation would require additional infrastructure, such as solar panels or energy-generating mechanisms. By adopting GNSS-R, Cubesats can effectively bypass these limitations and still gather essential geophysical data.

1.3 Specific challenges of Earth observation with Cubesats

1.3.1 Orbital constraints

From an orbital dynamics standpoint, employing Cubesats as a distributed sensor node network to achieve enhanced ground resolution presents numerous challenges related to orbital mechanics. At first, since the physics details will be covered later, this satellite network is set up in the following way: a central satellite moves in a circular orbit, while different secondary satellites orbit around it in a relative manner. To maintain this relative configuration around the central satellite, the absolute orbits of each secondary satellite must be slightly elliptical (or circular). A direct consequence of this ellipticity in the orbits is the variance in their angular rotation speeds, inevitably leading to a non-fixed configuration over time. This variability in the shape of the satellite configuration will need to be examined to ensure consistency in the outcomes extracted from Earth observation.

Another critical aspect to consider is the risk of collisions between the deputy satellites. In fact, an in-depth analysis conducted by Francesca Scala [26] aimed to understand the behavior of the formation in the presence of control failures. The analysis revealed a divergent motion pattern between the spacecrafts after a one-day period. This indicates that over time, without proper control, the spacecrafts will eventually drift apart, raising the potential for collisions or other unsafe scenarios. However, with the implementation of guidance, navigation, and control techniques, it was demonstrated that the current low-thrust technology is capable of maintaining formation stability, with control kept within the centimeter to millimeter range. Consequently, an onboard autonomous algorithm becomes essential for maneuvering, formation stability, and safe mode transitions.

Considering the standard dimensions of Cubesats used in this work, which typically measure 10 cm × 10 cm × 11 cm [23] and are equipped with sensors and antennas of approximately 10 cm on each side [31], the findings from Dr. Scala indicate that a minimum safe distance of about 15 cm between two Cubesats is necessary to prevent potential collisions in case of control failure. This distance was established by considering a safety threshold with a 40% margin between satellites.

An additional orbital limitation to take into account involves the challenge of keeping the Cubesats' plane locally parallel to the Earth's surface, specifically in cases of elliptical relative motion. This constraint will be examined in more depth in Section 3.1.1.4, as it will also have a notable influence on ground resolution.

1.3.2 Electromagnetic criteria

Once the mechanical constraints are understood, several criteria related to the electromagnetic aspects of the antennas need to be considered. As mentioned earlier, the use of Cubesats for Earth observation is advantageous due to their ability to carry each one element, which allows the use of the beamforming method. Beamforming is a spatial filtering technique employed to selectively receive signals arriving at an array of antennas from specific directions while reducing signal reception from other directions [19]. By focusing on these desired directions, beamforming creates main lobes, which represent the regions of optimal signal reception. By applying beamforming, it is possible to steer the main lobe towards the direction of interest. On the contrary, side lobes are generated as a byproduct of this process, representing areas of unwanted signal reception from directions outside the main lobes.

Therefore, the objective of this satellite formation, and thus the use of an antenna array, is to create a main beam that directly points towards the Earth's observation point, commonly known as the specular point. The width of this beam is inversely proportional to the ground resolution that the satellite swarm will provide, meaning that a very narrow beam will yield excellent resolution. However, each satellite configuration will impact the generated beam and, consequently, the ground resolution. As a reminder, resolution relates to the amount of information perceived by a satellite's sensor.

Several constraints must be considered. Firstly, the ground resolution should not exceed 1 kilometer, necessitating a very narrow beamwidth. Additionally, the glistening zone is considered to be a 5 kilometers radius disk and within this region, the presence of sidelobes must be addressed. Indeed, their presence in the glistening zone could cause interference, making it crucial to maintain them below -10 dB in this specific region.

In conclusion, the main objective of this thesis is to determine the most optimal configuration of Cubesats, considering orbital constraints, to achieve high ground resolution and minimizes sidelobes in the glistening zone. The number of satellites forming the constellations should be strategically selected, with a maximum limit set at 32 satellites, to balance cost considerations while always prioritizing a safe distance between them.

Chapter 2

State of the Art

Docking a pair of spacecraft is difficult, but flying multiple satellites in formation is a real challenge. The relative positions of the satellites must be maintained precisely to avoid collisions. The use of the equations of relative motion and an accurate understanding of their parameters will be essential to the research in this thesis.

2.1 Clohessy-Wiltshire equations

The Clohessy-Wiltshire (CW) equations provide a simplified representation of the relative motion of objects in orbit. In this model, the chief (or leading) object is assumed to be in a circular orbit around a celestial body, while the deputy (or secondary) object is in either a circular or elliptical orbit. The equations offer a basic approximation of the deputy's motion relative to the chief, and are expressed in a local coordinate system centered on the chief object. The model is frequently employed to plan and perform rendez-vous operations. However, this study focuses on its utilization for formation flight missions.

NASA engineers Robert H. Clohessy and Richard S. Wiltshire first introduced in the mid-20th century the equations that now carry their names [4]. Since then, these equations have been extensively studied and applied in a variety of space missions and applications. The original set of equations describes a simplified model for the orbital relative motion since it is based on several assumptions [9] [7] [27]:

1. **Circular leading orbit**: The chief body is assumed to be in a circular orbit around the Earth.
2. **Small relative motion**: The distance between the deputy body and the chief one is much smaller than the distance between the chief body and

the central celestial body they orbit around, such as Earth. This is an important assumption since the deputy's motion can be approximated as a linear function of time, and the equations can therefore be linearized.

3. **No third-body effects**: The gravitational effects of other bodies, such as the Moon or Sun, are not taken into account.

The well-known Clohessy-Wiltshire equations are:

$$\begin{cases} \ddot{x} = 2\omega\dot{y} + 3\omega^2 x + f_x \\ \ddot{y} = -2\omega\dot{x} + f_y \\ \ddot{z} = -\omega^2 z + f_z \end{cases} \tag{2.1}$$

The reference local frame used is known as the Hill-frame, denoted $\mathcal{H}$. The Hill-frame of the chief satellite is centered at its center of mass and is defined by the circular orbital plane of the chief satellite. This frame is rotating and moves along with the chief satellite according to the following conventions (depicted on Figure 2.1):

- $\hat{x}$: the radial axis, points radially away from the center of the celestial body.
- $\hat{y}$: the along-track axis, is tangent to the orbit and points in the direction of the satellite's velocity vector or the direction of its orbital motion.
- $\hat{z}$: the normal axis, completes the right-handed coordinate system by being normal to the orbital plane.

Additionally, $\omega = \sqrt{\frac{\mu}{a^3}}$ represents the reference orbit rate of the chief body, calculated as the square root of the standard gravitational parameter μ divided by the cube of the semi-major axis a of the chief's circular orbit. In the case of the chief orbiting in a circular orbit, ω simply denotes the chief body's mean motion. By extension, the semi-major axis a is the distance separating the center of the Earth from the chief satellite.

The external forces $\mathbf{f} = [f_x, f_y, f_z]^T$ are additional accelerations that affect the relative motion of the deputy satellite [17]. These forces arise due to aerodynamic effects, such as atmospheric drag, which can manifest when the satellite operates at altitudes where there is still some atmospheric resistance. However, this term encompasses various other influences, including third-body effects and thrust

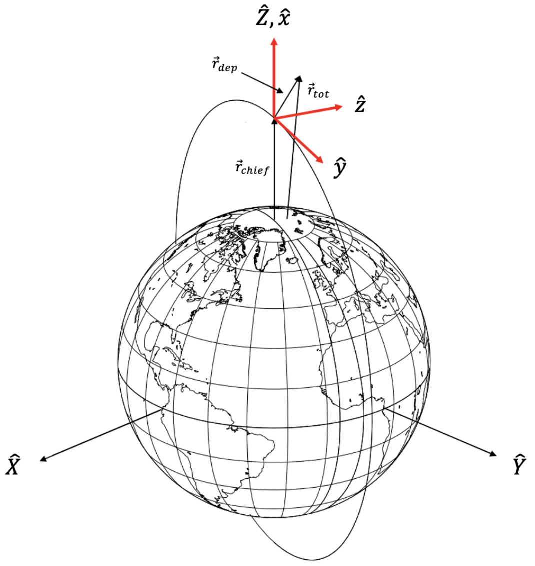

Figure 2.1: ECI $(\hat{X}, \hat{Y}, \hat{Z})$ and Hill $(\hat{x}, \hat{y}, \hat{z})$ coordinate systems [33]

commands [20]. Thus, the values of $\mathbf{f}$ depend on the shape and surface characteristics of the deputy satellite, as well as the properties of the surrounding atmosphere.

As already mentioned, it is essential to note that the Clohessy-Wiltshire equations are valid for relatively small relative distances and velocities, enabling an appropriate linearization of the relative motion. In more complex scenarios, where distances are larger, or other forces significantly influence the motion, more elaborate models and numerical resolution techniques may be required for higher precision in space formation flights.

2.2 General analytical solution of the CW equations

To solve this set of equations, it has been assumed an unperturbed case where no external forces are imparted by the deputy spacecraft, thus $\mathbf{f} = 0$. This means that any change in velocity (Δv) applied to the deputy satellite is considered to be instantaneous or impulsive. This assumption is useful because it simplifies the analysis by treating the change in velocity as a single event, allowing for straightforward calculations of the resulting velocity and position at that specific instant. It also means that the new velocity resulting from the Δv can serve as an initial condition for subsequent analysis.

2.2.1 x-component solution

David A. Vallado came up with an intuitive approach for tackling the CW equations that involves the use the Laplace operators [32]. The demonstration starts by taking the derivative of the x-equation while setting the external forces to 0.

$$\ddot{x} = 2\omega\dot{y} + 3\omega^2 x \qquad\qquad \dddot{x} \; = 2\omega + 3\omega^2\dot{x}\ddot{y} \tag{2.2}$$

Substitute $\ddot{y} = -2\omega\dot{x}$ into $\dddot{x}$ to obtain $\dddot{x} + \omega^2\dot{x}$. This is where the use of Laplace transforms comes in, which will allow the differential equations to be solved analytically (since converted into algebraic equations) and thus simplify the solutions:

$$\mathcal{L}\left[\, \dddot{x} + \omega^2\dot{x}\right] = \left\{s^3X(s) - s^2x_o - s\dot{x}_o - \ddot{x}_o\right\} + \omega^2\left\{sX(s) - x_o\right\} = 0 \tag{2.3}$$

This Laplace Transform can be developed and simplified to isolate $X(s)$:

$$\begin{aligned} &\Leftrightarrow s^3X(s) - s^2x_o - s\dot{x}_o - \ddot{x}_o + sX(s)\omega^2 - x_o\omega^2 = 0 \\ &\Leftrightarrow sX(s)(s^2+\omega^2) = (s^2+\omega^2)x_o + s\dot{x}_o + \ddot{x}_o \\ &\Longrightarrow X(s) = \frac{x_o}{s} + \frac{\dot{x}_o}{(s^2+\omega^2)} + \frac{\ddot{x}_o}{s(s^2+\omega^2)} \end{aligned} \tag{2.4}$$

In order to convert the given expression from the Laplace domain back to the time domain, it is recommended to decompose the last term using partial fractions.

$$\frac{\ddot{x}_o}{s(s^2+\omega^2)} = \frac{A}{s} + \frac{Bs+C}{s^2+\omega^2} \tag{2.5}$$

At this point, the 3 coefficients can be easily determined. A is found by evaluating the function around $s = 0$ and B and C by putting the right-hand side of the equation over a common denominator.

$$\begin{cases} \dfrac{\ddot{x}_o}{(s^2+\omega^2)} = A + \dfrac{Bs+C}{s^2+\omega^2}s \\ \dfrac{\ddot{x}_o}{s(s^2+\omega^2)} = \dfrac{A(s^2+\omega^2) + (Bs+C)s}{s(s^2+\omega^2)} \end{cases} \Longrightarrow \begin{cases} A = \dfrac{\ddot{x}_o}{\omega^2} \\ B = -\dfrac{\ddot{x}_o}{\omega^2} \\ C = 0 \end{cases} \tag{2.6}$$

The expression of $X(s)$ in the Laplace domain can therefore be expressed as:

$$X(s) = \frac{x_o}{s} + \frac{\dot{x}_o}{(s^2+\omega^2)} + \frac{\ddot{x}_o}{s\omega^2} - \frac{s\ddot{x}_o}{\omega^2(s^2+\omega^2)} \tag{2.7}$$

To take the inverse Laplace transform and arrive at the time-domain result, standard techniques for partial fraction decomposition and inverse Laplace transforms can be used, which end up with the following expression:

$$x(t) = x_o + \frac{\dot{x}_o}{\omega}\sin(\omega t) + \frac{\ddot{x}_o}{\omega^2} - \frac{\ddot{x}_o}{\omega^2}\cos(\omega t) \tag{2.8}$$

By substituting $\ddot{x}_o$ from the CW equations 2.1, still considering zero external forces, the first component of the general analytical solution can be obtained.

$$x(t) = x_o + \frac{3\omega^2 x_o + 2\omega\dot{y}_o}{\omega^2} + \frac{\dot{x}_o}{\omega}\sin(\omega t) - \frac{3\omega^2 x_o + 2\omega\dot{y}_o}{\omega^2}\cos(\omega t) \tag{2.9}$$

$$\implies x(t) = \left(4x_o + \frac{2\dot{y}_o}{\omega}\right) + \frac{\dot{x}_o}{\omega}\sin(\omega t) - \left(3x_o + \frac{2\dot{y}_o}{\omega}\right)\cos(\omega t) \tag{2.10}$$

2.2.2 y-component solution

Having established the x-component solution, the y-component solution can be directly derived by revisiting the CW equations 2.1 and substituting them with the derivative of equation 2.10.

$$\begin{aligned} &\Leftrightarrow \ddot{y} = -2\omega\dot{x} \\ &\Leftrightarrow \ddot{y} = -2\omega\left[\dot{x}_o\cos(\omega t) + (3\omega x_o + 2\dot{y}_o)\sin(\omega t)\right] \\ &\Leftrightarrow \ddot{y} = -2\omega\dot{x}_o\cos(\omega t) - 2\omega\left(3\omega x_o + 2\dot{y}_o\right)\sin(\omega t) \end{aligned} \tag{2.11}$$

Consequently, the y-component can be obtained by double integrating the last expression of $\ddot{y}$.

- $\dot{y} = -2\dot{x}_o\sin(\omega t) + 2\left(3\omega x_o + 2\dot{y}_o\right)\cos(\omega t) + C$
- $y = \frac{2\dot{x}_o}{\omega}\cos(\omega t) + \left(6x_o + \frac{4\dot{y}_o}{\omega}\right)\sin(\omega t) + Ct + D$

where the derivation of the constant of integration is basically achieved by evaluating the $\dot{y}$ and y equations around $t = 0$:

$$\begin{cases} \dot{y}_o = 6\omega x_o + 4\dot{y}_o + C \\ y_o = \dfrac{2\dot{x}_o}{\omega} + D \end{cases} \implies \begin{cases} C = -6\omega x_o - 3\dot{y}_o \\ D = -\dfrac{2\dot{x}_o}{\omega} + y_o \end{cases} \tag{2.12}$$

The second component of the general analytical solution finally appears to be:

$$y(t) = \left(y_o - \frac{2\dot{x}_o}{\omega}\right) + \left(6x_o + \frac{4\dot{y}_o}{\omega}\right)\sin(\omega t) + \frac{2\dot{x}_o}{\omega}\,\mathrm{Cos}(\omega t) - (6\omega x_o + 3\dot{y}_o)\,t \tag{2.13}$$

2.2.3 z-component solution

The z-component equation has a straightforward solution as it is not coupled with the 2 other CW equations. It is commonly recognized as a simple harmonic oscillator. The use of Laplace transform is again effective:

$$\begin{aligned} &\mathcal{L}\left[\ddot{z} + \omega^2 z\right] = s^2 Z(s) - s z_o - \dot{z}_o + \omega^2 Z(s) = 0 \\ &\implies Z(s) = \frac{s z_o}{(s^2 + \omega^2)} + \frac{\dot{z}_o}{(s^2 + \omega^2)} \end{aligned} \tag{2.14}$$

From which the expression in the time domain of the third component of the general analytical solution can be directly deduced:

$$z(t) = z_o \cos(\omega t) + \frac{\dot{z}_o}{\omega}\sin(\omega t) \tag{2.15}$$

2.3 Reformulation of the general analytical solution

It the case of this thesis, it is convenient to express the analytical solutions of the CW equations in terms of shape, size and position of the relative orbit [32]. Indeed, the expressions generated in Section 2.2 may seem complex to analyse. Thus, it appears necessary to provide a rewording that assigns physical significance to the different variable parameters and facilitates comprehension of their effects.

Still based on the work of David A. Vallado [32], the idea is to introduce some definitions, which will appear to have significant meaning at the end, such as this parameter C, to simplify the expression of the equations:

$$C \equiv \sqrt{\left(3x_o + \frac{2\dot{y}_o}{\omega}\right)^2 + \left(\frac{\dot{x}_o}{\omega}\right)^2} \tag{2.16}$$

This parameter, which represents the magnitude of oscillation as it will become clearer later, can be incorporated into the x-component expression:

$$x(t) = C\left\{\frac{\frac{\dot{x}_o}{\omega}}{C}\sin(\omega t) - \frac{3x_o + \frac{2\dot{y}_o}{\omega}}{C}\cos(\omega t)\right\} + 4x_o + \frac{2\dot{y}_o}{\omega} \tag{2.17}$$

where the two trigonometric terms are described as:

$$\sin(\psi_o) \equiv -\frac{3x_o + \frac{2\dot{y}_o}{\omega}}{C} \qquad \cos(\psi_o) \equiv \frac{\frac{\dot{x}_o}{\omega}}{C} \tag{2.18}$$

By substituting the given values into the x-component equation and apply the trigonometric summation identity[1], the equation can be simplified. Similar operations can be performed on the y and z-component equations to obtain the desired result. The only difference for the z-solution is to determine the magnitude of oscillation as $D = \sqrt{(\frac{\dot{z}_o}{\omega})^2 + z_o^2}$. The reformulation of the CW analytical solution which provide a better geometric insight result in:

$$\begin{cases} x(t) = x_{\text{off}} + C\sin(\omega t + \phi_o) \\ y(t) = y_{\text{off}_o} + \dot{y}_{\text{off}}t + 2C\cos(\omega t + \phi_o) \\ z(t) = D\cos(\omega t - \theta_o) \end{cases} \tag{2.19}$$

where C and D are the amplitudes of the cyclic in-plane (or semi-minor axis of the relative orbit) and out-of-plane motion respectively, ϕ_o and θ_o are the associated phase angles, and x_{off} and y_{off_o} are the orbit radial and along-track offsets. It is important to understand the meaning of the y_{off_o} notation. Indeed, the drift term, $\dot{y}_{\text{off}}$, introduces a linear component to the motion of the deputy satellite in the relative frame, causing it to deviate from a purely elliptical orbit. However, it has important implications for the relative motion of the satellites. It affects the shape and size of the relative orbit, causing it to gradually change over time. The

---

[1] Trigonometric summation identity : $\sin(a + b) = \sin(a)\cos(b) + \cos(a)\sin(b)$

magnitude of the drift term determines the rate at which the deputy satellite drifts away from the chief satellite. Hence, the presence of a 0 index in the y-offset comes directly from the fact that the orbit is instantaneous. Because of this drift term, which evolves with time, the y-offset is only valid for $t = 0$.

Therefore, it can be useful to determine this drift term in terms of initial conditions. The drift term can be expressed as a function of x_o and $\dot{y}_o$ as:

$$\dot{y}_{\text{off}} = -6\omega x_o - 3\dot{y}_o \tag{2.20}$$

Then, the initial displacement terms, which give the initial position of the center of the relative orbit, can be determined based on equation 2.17 and the expression of the drift term:

$$\begin{aligned} x_{\text{off}} &= 4x_o + \frac{2\dot{y}_o}{\omega} \\ &= -\frac{2\dot{y}_{\text{off}}}{3\omega} \end{aligned} \qquad y_{\text{off}_0} = y_o - \frac{2\dot{x}_o}{\omega} \tag{2.21}$$

Additionally, it is important to observe that the equations for $x(t)$ and $z(t)$ remain constant as they are solely determined by the initial conditions. This implies that there is no displacement or drift in the x and z directions.

Finally, the relative state vector of system 2.19 is defined by eight initial conditions $(x_o, \dot{x}_o, y_o, \dot{y}_o, z_o, \dot{z}_o, \phi_o, \theta_o)$ that describe the unperturbed motion of a secondary object around a leading one. These conditions offer convenient scaling and phasing terms that allow for the direct manipulation and shaping of the relative orbit [2].

Chapter 3

Orbital Dynamics

This chapter provides an overview of the development stages and methodology employed in the mechanical part of this project. The methodology is structured around two main axes: the investigation of relative motion within a relative frame of reference and the alignment of this relative system within an absolute geocentric frame.

3.1 Relative Orbital Dynamics

This section seeks to determine the challenges associated with orbital mechanics in a local reference frame. It involves analyzing the Clohessy-Wiltshire equations to understand their structure and developing a series of satellite configurations compliant with the laws of physics. To accomplish this, the relative reference coordinate system mentioned in Section 2.1 will be utilized throughout this section, serving as the foundation for the analysis.

3.1.1 Trend analysis of the CW equations

Analyzing the trends of the CW equations will be beneficial when arriving to optimize formation flights. By manipulating the eight initial conditions and studying their impact on the relative motion, it becomes possible to create a wide range of formations with different shapes and configurations. This understanding will prove to be crucial to design the most suitable formation for the specific project requirements.

3.1.1.1 Kill the drift

Section 2.3 highlighted the presence of drift in the relative motion of a deputy satellite with respect to the lead satellite. However, in order to sustain formation flying over an orbital period, eliminating this drift is of paramount importance. Hence, solving equation 2.20 will provide a solution for $\dot{y}_o$ that cancels out the drift value:

$$\dot{y}_o = -2\omega x_o \tag{3.1}$$

Subsequently, it is shown in Figure 3.1b that by nullifying this y-directional drift, the relative motion of a deputy satellite around the chief one adopts an elliptical pattern.

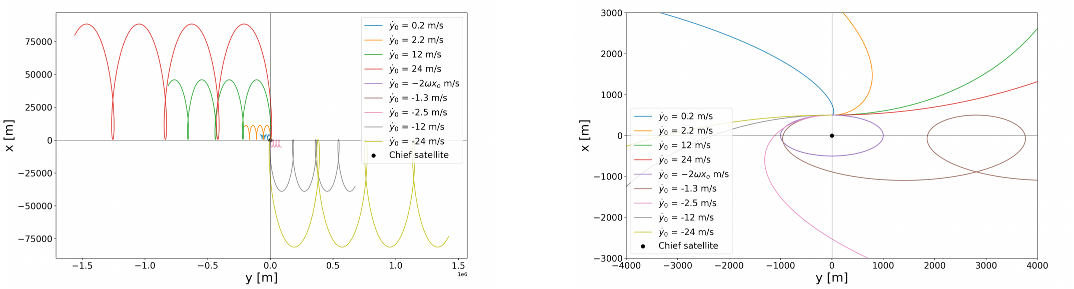

(a) Overall situation: relative drift

(b) Close-up view: cancellation of drift

Figure 3.1: (a) Overall evolution of the motion showing the emergence of drift, and (b) Close-up view revealing the cancellation of drift and transition to elliptical motion at a specific $\dot{y}_o$.

3.1.1.2 Chief centered motion and influence of x_o

Currently, the focus is on working in a relative frame of reference centered on the chief satellite. The simplest approach would be to consistently position the center of the ellipse followed by the deputy satellites at the origin of this relative frame. However, as it has been previously observed (cfr. equation 2.21), the position in the x-direction of the center of the relative elliptical orbit only depends on the y-direction drift. Nevertheless, as the objective is to get rid of this drift, the relative orbit will always be centered at $x = 0$.

In the y-direction, the situation is slightly more complex. Referring back to equation 2.21, it can be directly observed a dependence on y_o and $\dot{x}_o$. To guarantee to always achieve a relative orbit centered on the chief satellite, regardless of the variable parameter values, y_o can simply be set at:

$$\begin{aligned} y_o &= y_{off} + \frac{2\dot{x}_o}{\omega} \\ &= \frac{2\dot{x}_o}{\omega} \end{aligned} \tag{3.2}$$

This will always ensure the desired centering in the y-direction. The proof has been depicted on Figure 3.2.

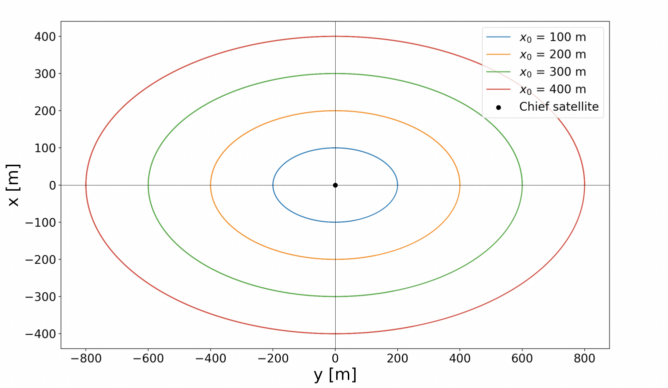

Figure 3.2: Chief centered motion for different x_o, setting $\dot{y}_o = -2\omega x_o$, $y_o = \frac{2\dot{x}_o}{\omega}$ and $\dot{x}_o = 0$.

Another interesting conclusion that can be drawn from this graph is the influence of the x_o parameter. As it is clearly shows, the x_o value directly gives the semi-minor axis of the relative orbit around the leading satellite (considering no burn in the x-direction). This can be mathematically explained taking back equation 2.16 and substituting the expression of $\dot{y}_o$ to kill the drift:

$$\begin{aligned} C &= \sqrt{(3x_o - \frac{4\omega x_o}{\omega})^2 + (\frac{\dot{x}_o}{\omega})^2} \\ &= \sqrt{(-x_o)^2 + (\frac{\dot{x}_o}{\omega})^2} \end{aligned} \tag{3.3}$$

where the impact of x_o and $\dot{x}_o$ becomes evident on the magnitude of the oscillations.

3.1.1.3 Phase shift

The calculation of relative elliptic trajectories of the deputy satellites in the x-y plane being more apparent, it is necessary to consider the fifth variable parameter, the phase shift (ϕ_o). Rather than solely concentrating on the overall trajectory, it becomes essential to consider the individual positions of the satellites along the orbit. The phase shift is particularly valuable in positioning multiple satellites on the same relative orbit while avoiding collisions. Additional phase shifts can also be introduced between different relative orbits to create intricate configurations, such as spiral formations (cfr. Section 3.1.2.3).

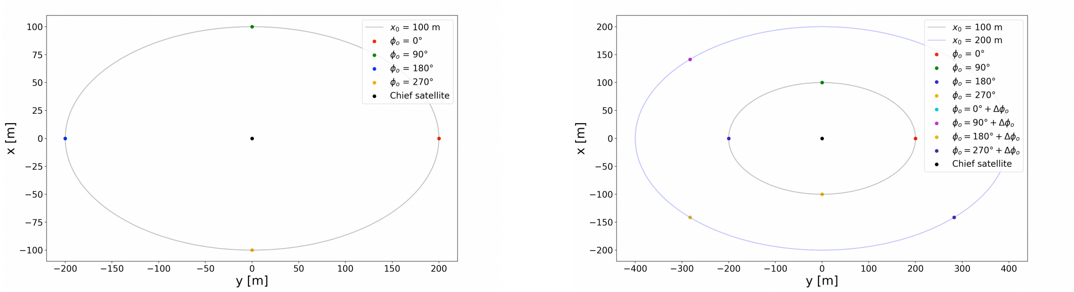

(a) Constant phase shift of 90°

(b) Extra 45° phase shift for second orbit

Figure 3.3: Phase shift illustration for satellite placements on similar orbits.

3.1.1.4 Tilt in the z-direction

The understanding of the three last initial conditions ($z_o, \dot{z}_o$ and θ_o) is easier since they are not coupled with the 2 other directions. Therefore, it can be directly observed on Figure 3.4a that adding any initial z displacement or velocity creates a spiral motion out of the x-z plane.

To eliminate the oscillatory movement, it is once again necessary to apply equation 3.1. This results in an elliptical orbit titled at an angle of 45° around the x-axis. However, the orbital plane can be rotated around the z-axis by introducing a phase shift, θ_0, as depicted on Figure 3.4b.

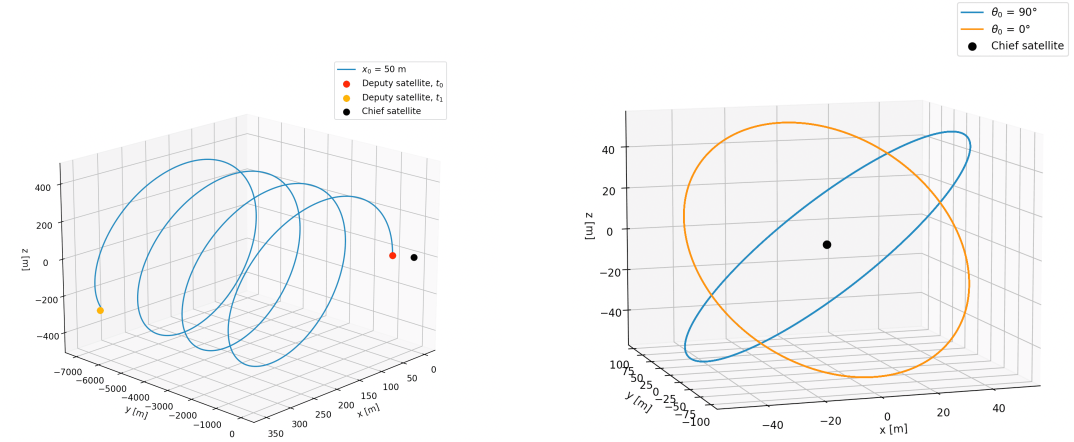

(a) Oscillatory motion

(b) Rotation around z-axis

Figure 3.4: (a) Illustration of the oscillatory motion with added z-component. (b) Eliminating the oscillatory component to achieve elliptical orbits. Additionally, the feasibility of shifting the orbit inclination is shown.

Moreover, if multiple concentric orbits are desired for the relative motion of satellites, it is crucial to maintain them within the same plane. This can be achieved by enforcing the condition that the value of z_o remains consistently equal to the value of x_o (this condition also applies to $\dot{z}_o$ and $\dot{x}_o$). Nevertheless, the value of z_o can be changed as long as it remains a multiple of x_o. However, this will have consequences on the shape of the elliptical orbits. Specifically, it will significantly elongate the satellite configuration, stretching the minor axis while leaving the major axis unchanged in length. Moreover, the augmentation of z_o will have a direct effect on the inclination of the orbital plane. In essence, when z_o is increased, the configuration stretches along the minor axis, causing an increase in inclination relative to the x-y plane. This phenomenon is depicted in Figure 3.5 for an arbitrary spiral configuration with the alteration of only the z_0 value.

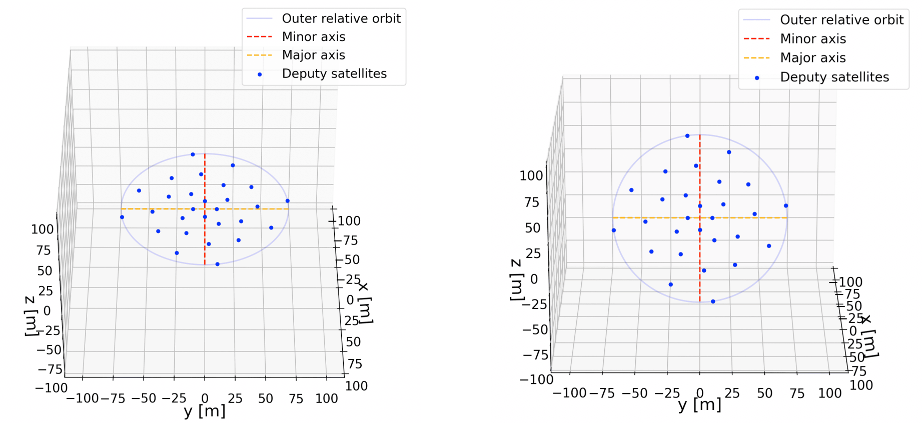

(a) 3D tilting for $z_0 = x_0$

(b) 3D tilting for $z_0 = 2x_0$

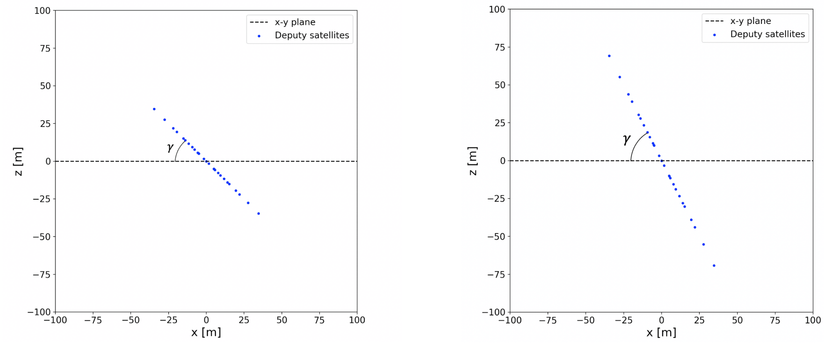

(c) $z_0 = x_0$: $\gamma = 45°$ tilt

(d) $z_0 = 2x_0$: $\gamma = 64°$ tilt

Figure 3.5: Satellite constellation with doubled z_0, stretching the vertical axis while keeping the horizontal axis unchanged (a and b). The resulting change in tilt relative to the x-y plane is also depicted (c and d).

The study of satellite plane inclination in the z-direction involves a fundamental orbital constraint to be considered in this work. After nullifying the drift, a three-dimensional elliptical motion emerges at a 45° inclination. This 45° inclination can be rotated around the z-axis by adding a phase shift θ_0. This inclination can also be accentuated by increasing the value of z_0, directly impacting the elongation of the satellite configuration. However, despite these two degrees of freedom in the z-direction, it is important to emphasize that physics will not permit positioning the CubeSats formation plane locally parallel to the Earth's surface (in the y-z plane). As a result for future analyses, the satellite constellation involving elliptical relative orbits will consistently exhibit local inclination relative to the Earth's surface.

3.1.2 Determination of formation flights

By manipulating the eight different initial conditions explored in the previous section, an infinite number of satellite positions can be calculated, each resulting in unique flight formations. However, it's important to keep in mind the physical constraints imposed by the equations of CW. In the framework of this thesis, a small number of these formations have been studied. Those are considered the most relevant and likely to yield good results in the analysis phase.

- **Single Orbit Formation**: In this formation, the Cubesats orbit around the leading satellite in a single relative elliptical orbit. They are spaced from each other by a constant distance.

- **Symmetrical Orbit Formation**: The Cubesats are arranged in a symmetrical pattern around the chief satellite, with two distinct orbits up and downstream the chief satellite.

- **Concentric Orbit Formation**: Distributed across multiple relative concentric orbits, the Cubesats form a spiral with a variable number of arms.

- **Y Formation**: The Cubesats are configured in a "Y" shape around the chief satellite, reminiscent of the arrangement seen in the VLA radio telescope [34].

Each of these flight formations requires a specific selection of the eight variable parameters of the CW equations for each satellite. The implementation of such configurations is described subsequently.

3.1.2.1 Single Orbit Formation

In the single orbit formation, all the Cubesats orbit around the chief satellite, following the same relative elliptical trajectory. They maintain a constant distance from each other, creating a cohesive formation. The chief satellite acts as the central reference point, around which the Cubesats navigate.

To obtain such a configuration, the drift must be killed (cfr. Section 3.1.1.1) and the x_o and y_o parameters are such that the elliptical orbit is centered at 0 (cfr. Section 3.1.1.2). Additionally, a constant phase shift, ϕ_o, is applied (cfr. Section 3.1.1.3) while the variable x_o controls the size of the singular orbit.

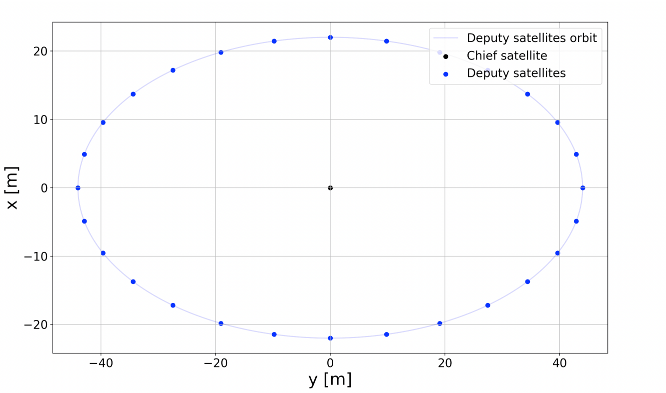

Figure 3.6: Single orbit formation of 29 satellites around the chief one.

3.1.2.2 Symmetrical Orbit Formation

This configuration demonstrates how the CW equations enable achieving a relative elliptical motion of Cubesats positioned both ahead of and behind the chief satellite in the direction of motion (y-direction). This becomes possible due to the fact that the center position of a relative orbit along the y-axis depends on y_0 and $\dot{x}_0$ (see equation 2.21). Unlike the offset along the x-axis, which cancels out for an elliptical relative motion (cfr. Section 3.1.1.2). Therefore, this specific symmetrical configuration can not be realized in the radial direction (x-direction) with the relative orbits positioned above or below the chief satellite.

A third dimension can be added using z_0 or $\dot{z}_0$. As shown in Figure 3.7b, the relative motion of the satellites remains in a plane (the x-y plane), but the individual rotation orbits of each Cubesat will be inclined, creating this mesh-like pattern that represents the relative orbits of each satellite over time.

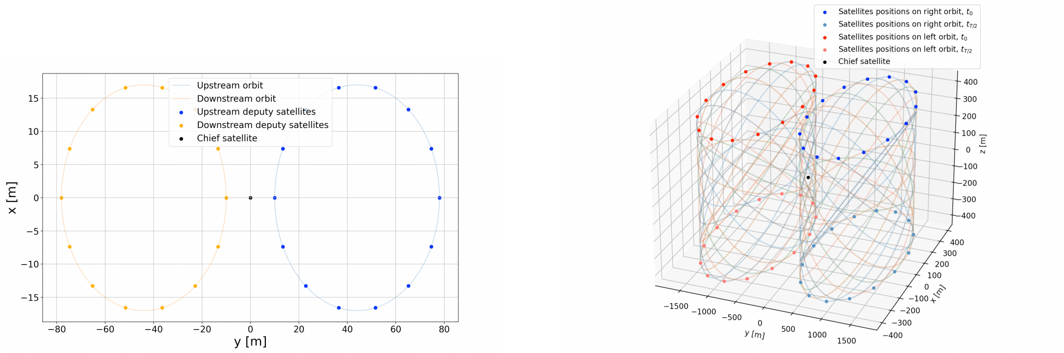

(a) 2D symmetrical orbits formation

(b) 3D symmetrical orbits formation

Figure 3.7: Symmetrical relative movement in (a) 2D and (b) 3D of the deputy satellites in two different orbits upstream and downstream of the leading satellite in the direction of motion (y-direction).

3.1.2.3 Spiral Formation

In Figure 3.8, the placement of Cubesats over different concentric orbits is depicted, resulting in a spiral configuration. The initial conditions of the CW equations are identical to those in the single orbit formation, with the exception that an additional phase shift is introduced when transitioning to a different elliptical orbit (such as demonstrated in Figure 3.3b).

This visualization provides a clear representation of the spiral formation and highlight the careful arrangement of the Cubesats along concentric orbits. The blue lines trace the path followed by the satellites during a full orbital cycle, showing the gradual evolution of the formation over time.

There are two interesting aspects to consider in this configuration. Firstly, the number of arms in the spiral formation can be varied, providing flexibility in the design. Figure 3.8 illustrates configurations with 2 arms (3.8a), 4 arms (3.8b) and 5 arms (3.8c). However, it's important to note that the number of arms is not limited, except by the maximum number of satellites that can be deployed. This allows for a wide range of possibilities when it comes to the formation's structure and geometry.

The second advantage lies in the capability of this type of configuration to cover a significant area. By adjusting the semi-major axis of the relative orbits and introducing phase shifts between each orbit, the formation can cover an wide elliptical range. Additionally, this flexibility allows for precise adjustment of satellite density.

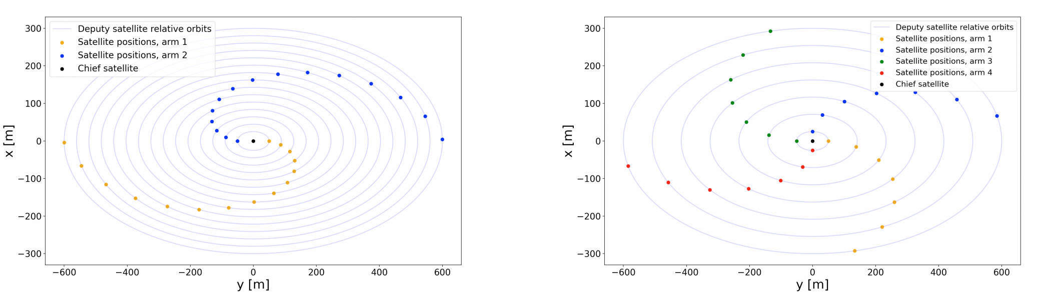

(a) 2 arms spiral (b) 4 arms spiral

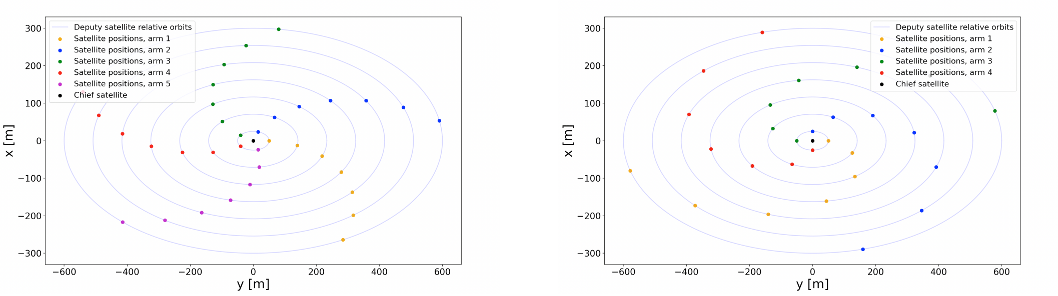

(c) 5 arms spiral (d) 4 arms spiral + additional phase shift

Figure 3.8: Spiral formation using concentric relative orbits with (a) 31 satellites (b) 29 satellites (c) 31 satellites (d) 29 satellites and an additional phase shift between concentric orbit.

3.1.2.4 Y-shaped Formation

The Y-shaped formation positions satellites to form the shape of the letter 'Y' around the chief satellite, located at the center of the Y where the two arms intersect. These two arms extend symmetrically outward from the chief satellite in different directions, with multiple satellites evenly spaced along each arm. However, to prevent collisions between satellites during movement, the position of Cubesats along the two arms are slightly offset with respect to each other.

This configuration is achieved by eliminating any motion in the x-direction. This is accomplished by setting x_o, $\dot{x}_o$, and $\dot{y}_o$ to 0 (cfr. Sections 3.1.1.1 and 3.1.1.2). Consequently, the positioning can only be achieved using y_o, while the arm spacing is determined by z_o. The satellite constellation takes place inevitably in the y-z plane, and no longer in the x-y plane as in the previous studied configurations. In this particular formation, the Cubesats formation plane is locally parallel to the Earth's surface.

The Y formation offers advantages in terms of coverage. With satellites distributed along the arms, the formation can effectively cover a wide area or specific regions of interest. The asset being the possibility to enlarge the size of the arms as well as to vary their opening.

Figure 3.9 illustrates the arrangement of 25 satellites around the chief satellite in the Y-shaped formation. The initial positions of the satellites are represented by blue dots, while their positions after half an orbital period ($T/2$) are shown in orange, indicating their maximum displacement in the z-direction. The blue lines depict the range of motion for the satellites throughout one complete orbital period.

As the orbital period progresses, the satellites gradually converge, forming a single line at the quarter and three-quarter marks of the orbital period. The amplitude of the arms is at its maximum at the initial time and halfway through the orbital period.

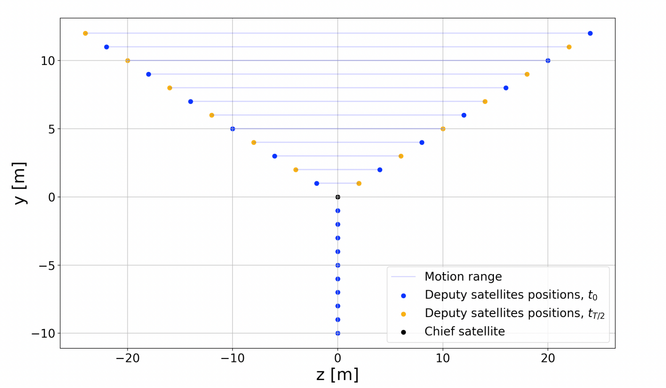

Figure 3.9: Y-shaped formation of 25 satellites with a constant and arbitrary initial z-displacement increment set at 2 [m]

3.2 Absolute Orbital Dynamics

Now that the study of formations in a relative local reference frame has been explored, it is essential to develop a methodology for maintaining this relative motion within an absolute coordinate system centered on Earth. This section delves into all aspects related to the absolute orbital mechanics of the Cubesat swarm. Beyond sustaining the configuration's absolute motion in a geocentric frame, particularly during a formation flight aimed at observing the Earth, it is crucial to maintain the satellite plane continuously oriented towards the Earth. Hence, the first part of this section will focus on formulating a model that integrates a Hill frame into an inertial geocentric frame. The second part will address the computation of the specular point once the formation is in orbit.

3.2.1 Absolute motion

This section is intended to demonstrate the possibility to express a relative motion into an inertial frame [25]. Indeed, to describe the absolute motion of the deputy satellites around the Earth, two systems of coordinates are needed: an inertial one and a local one. The state vector in the inertial system, which is fixed to the Earth, describes the absolute motion of a chief satellite with respect to the Earth. The local frame is fixed to the formation and thus able to describe the relative distances and velocities between the deputy satellites.

3.2.1.1 Inertial frame

The inertial frame used in this work is the Earth-centred inertial (ECI) coordinate system, denoted $\mathcal{I}$. In the specific case of this study, the orientation of the different axes is not important since the Earth rotation has not been taken into account. According to convention, it is typically expected that the $\hat{X}$ and $\hat{Y}$ axes lie in the Earth's equatorial plane, while the $\hat{Z}$-axis points towards the North Pole.

To consider the effects of the Earth's rotation, the $\hat{X}$-axis should be indicated as pointing towards the vernal equinox[1]. By doing so, the orthogonal coordinate system is completed by the $\hat{Y}$-axis.

3.2.1.2 Local frame

As already described in Chapter 2, when observing a deputy satellite from the perspective of the chief satellite, the reference local frame used is the Hill-frame,

---

[1] The vernal equinox is one of the two points in the sky where the ecliptic (the Sun's annual pathway) and the celestial equator intersect [3].

denoted $\mathcal{H}$. This frame is in constant rotation and accompanies the chief satellite's motion. Recalling the convention of this relative frame:

- $\hat{x}$: the radial axis, points radially away from the center of the celestial body.
- $\hat{y}$: the along-track axis, is tangent to the orbit and points in the direction of the satellite's velocity vector or the direction of its orbital motion.
- $\hat{z}$: the normal axis, completes the right-handed coordinate system by being normal to the orbital plane.

3.2.1.3 Hill to ECI frame transformation

Assuming that the position and velocity vectors of the chief satellite in the $\mathcal{I}$-frame are denoted as $\mathbf{r_{chief}}$ and $\mathbf{v_{chief}}$ respectively, the corresponding vectors $\mathbf{r_{dep}}$ and $\mathbf{v_{dep}}$ are applicable to the deputy satellite, but this time in the $\mathcal{H}$-frame. Therefore, as it is clearly depicted on Figure 2.1, the origin of the $\mathcal{H}$-frame is located at a distance $\|\mathbf{r_{chief}}\|$ from the $\mathcal{I}$-frame origin.

To perform such a transformation between the Hill frame and the ECI one, a rotation matrix must be computed:

$$\hat{\mathbf{x}}^{\mathcal{H}} = \frac{\mathbf{r}^{\mathcal{I}}_{\mathbf{chief}}}{\|\mathbf{r_{chief}}\|^{\mathcal{I}}} \qquad \hat{\mathbf{z}}^{\mathcal{H}} = \frac{\mathbf{r}^{\mathcal{I}}_{\mathbf{chief}} \times \mathbf{v}^{\mathcal{I}}_{\mathbf{chief}}}{\|\mathbf{r_{chief}} \times \mathbf{v_{chief}}\|^{\mathcal{I}}} \qquad \hat{\mathbf{y}}^{\mathcal{H}} = \hat{\mathbf{x}}^{\mathcal{H}} \times \hat{\mathbf{z}}^{\mathcal{H}} \tag{3.4}$$

The directional transformation matrix can be obtained as follow:

$$\mathbf{R} = \begin{bmatrix} \hat{\mathbf{x}}^{\mathcal{H}} & \hat{\mathbf{y}}^{\mathcal{H}} & \hat{\mathbf{z}}^{\mathcal{H}} \end{bmatrix}^T \tag{3.5}$$

This rotation matrix can finally be applied to the position and velocity vectors of the deputy satellite in the local frame to obtain their values in the inertial frame:

$$\mathbf{r}^{\mathcal{I}}_{\mathbf{dep}} = \mathbf{R} \cdot \mathbf{r}^{\mathcal{H}}_{\mathbf{dep}} \qquad \mathbf{v}^{\mathcal{I}}_{\mathbf{dep}} = \mathbf{R} \cdot \mathbf{v}^{\mathcal{H}}_{\mathbf{dep}} \tag{3.6}$$

The position of the deputy satellite in the absolute frame is now computable by simply summing the 2 position components in the inertial frame:

$$\mathbf{r_{tot}} = \mathbf{r}^{\mathcal{I}}_{\mathbf{chief}} + \mathbf{r}^{\mathcal{I}}_{\mathbf{dep}} \tag{3.7}$$

3.2.2 Specular point

The purpose of this section is to demonstrate the calculation of the specular point, which represents the ground point that corresponds to the shortest distance between the GNSS satellite and the Earth's surface, and between the Cubesat swarm and the Earth's surface. As previously described, the GNSS-Cubesat system operates based on electromagnetic waves transmitted from the GNSS satellite, which are reflected off the Earth's surface. The point where this reflection occurs is the specular point. This signal is then received by the Cubesats swarm in low Earth orbit. For simplicity in this thesis, the Earth is approximated as a spherical shape.[2]

To achieve the most realistic conditions, a circular low Earth orbit at an altitude of 400 kilometers was considered for the chief satellite of the Cubesat swarm. A polar orbit with an inclination of 90° relative to the equatorial plane and a Right Ascension of the Ascending Node [3] and an argument of perigee [4] equal to zero were selected. In this type of orbit, the orbital plane coincides with the Earth's meridian plane, and the satellites pass over the North and South poles in each revolution.

As for the GNSS, the Galileo satellite was considered. Developed by the European Union and the European Space Agency (ESA), Galileo aims to provide high-precision global navigation services and therefore serves as an excellent candidate. Each Galileo satellite orbits at an average altitude of 23 222 km in three distinct orbital planes, each with an inclination of 56° [12].

Note that the calculation of the specular point remains applicable regardless of the chosen orbit for the Cubesats' formation and the GNSS satellite. These conditions were employed to provide an illustrative example of the method's utilization, using parameters close to those encountered in practical scenarios.

---

[2] Preliminary work has already been carried out by a former student, Ugo-Paul Durafour, to model the real Earth using spherical harmonics [10].

[3] The right ascension of the ascending node (RAAN) is one of the 6 Keplerian orbital elements required to identify a specific orbit. It is the angle measured between the vernal equinox direction and the ascending node, or the point where a satellite crosses the equator moving upward from south to north. In other words, it describes the longitude orientation of the orbital plane in inertial space [15].

[4] The Argument of Perigee (argp) is one of the 6 Keplerian orbital elements required to identify a specific orbit. It represents the angle between the ascending node and the periapsis point of the orbit [14].

3.2.2.1 Satellite line-of-sight

A first approach in calculating the specular point is to ensure that both satellites are within the same field of view. Indeed, depending on the orbits and angular velocities of the objects, it is common for the Earth to obstruct the line of sight between the two satellites, preventing them from seeing each other.

In this case, the approximation of a spherical Earth simplifies the calculations. To determine whether two satellites are visible to each other, a line between the two objects can simply be drawn and, combined with the equation of a sphere, it is possible to determine if the line intersects the sphere. If the equation has one or two roots, indicating one or two intersections between the line and the sphere, it means that the Earth obstructs the line of sight between the two satellites. If the equation has no roots, it means that the satellites are visible to each other.

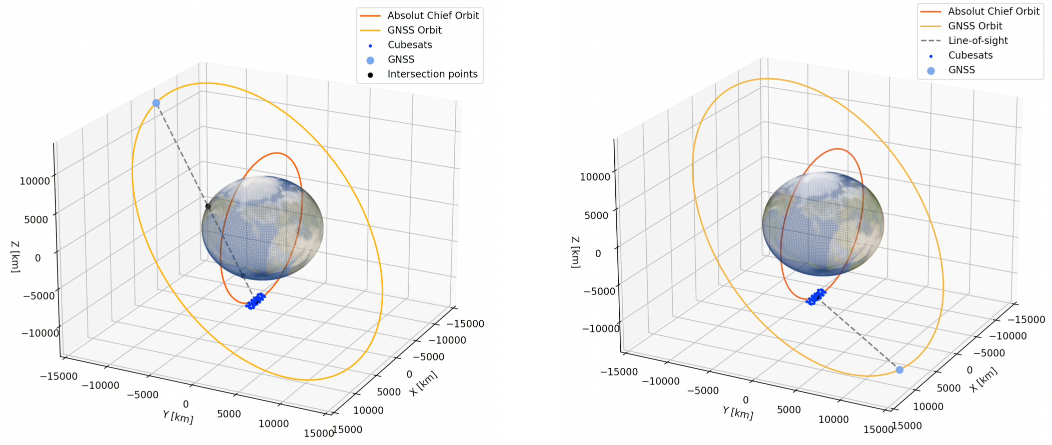

(a) Intersection points

(b) No intersection points

Figure 3.10: Graphical representation of the GNSS and Cubesats swarm: (a) obstructed by the Earth, and (b) in direct line-of-sight.

3.2.2.2 Computation of specular points

Once it has been ensured that the two satellites are within the same field of view, it becomes possible to calculate the specular point on the Earth's surface. As previously mentioned, the specular point represents the point on Earth that minimizes the sum of distances d1 and d2 in Figure 3.11. To calculate this, the use of a Python function simplifies the process. Specifically, the `minimize()` function is part of the *scipy.optimize* module in Python [28]. It is designed to numerically minimize a given objective function while considering constraints. In this case, the objective function is to minimize the sum of d1 and d2, with the constraint that the point lies on the spherical surface of the Earth.

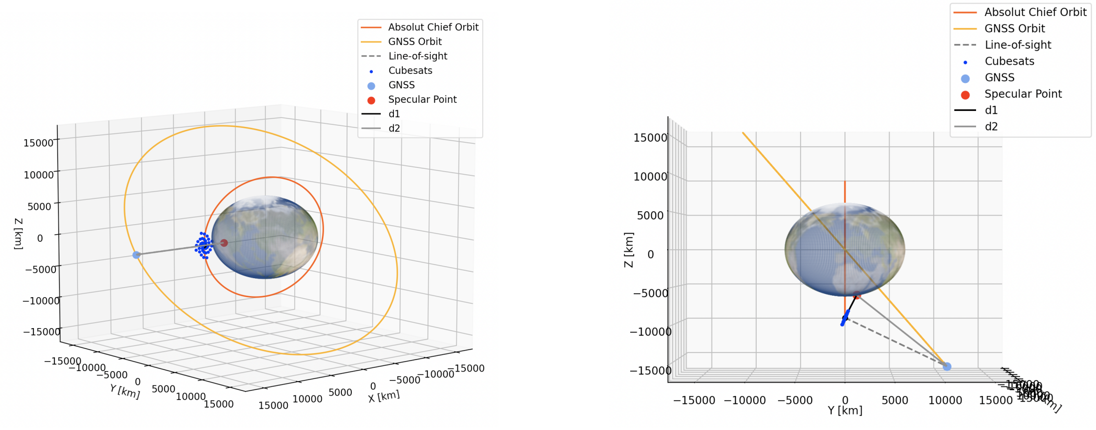

(a) Starting position

(b) Quarter of the orbital period

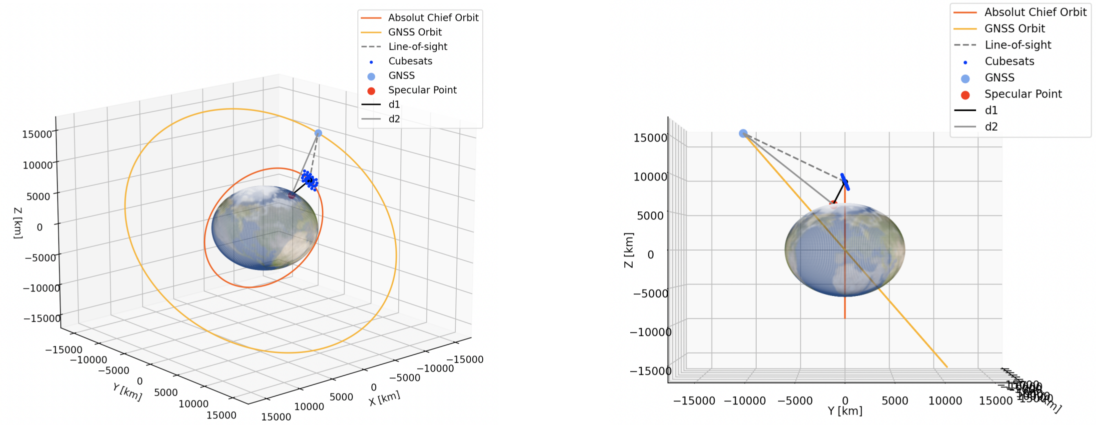

(c) 3/5 of the orbital period

(d) Three quarters of the orbital period

Figure 3.11: Evolution of the specular point with the position of the satellites

To ensure the accuracy of the specular point calculation, an additional verification can be performed by comparing the angle of incidence to the angle of reflection. This verification is based on the principle of reflection, which states that the angle at which a ray of light strikes a surface is equal to the angle at which the reflected ray departs from the surface, measured relative to the surface normal [1]. Verifying the equality of these angles provides an extra assurance regarding the accuracy of the specular point calculation using the Python function.

Chapter 4

Electromagnetic Analysis

This chapter aims to develop comparison tools that will be subsequently utilized to perform an initial analysis of Cubesat configurations. This analysis is carried out to extract the general trends from different configurations, leading to the identification of those that will produce optimal results.

4.1 Comparison tools

So far, the research for this project has focused on orbital mechanics, which has enabled the identification of feasible types of formation flight based on the laws of physics. Now, to conduct an analysis of these different configurations and determine which one is superior to the others, the need for comparative tools arises. Consequently, from now on, the emphasis will shift towards the electromagnetic aspect of the project and the formations of Cubesats will be considered as antenna arrays.

The first developed tool for comparison is the radiation pattern, which will help visualize the different emission lobes of the antenna arrays, particularly the main lobe of interest. Following this, the calculation of ground resolution and the glistening zone will be developed to verify that the configurations meet the two constraints in terms of resolution and sidelobes (cfr. Section 1.3). Lastly, the concept of ground spot will be explained for application in Chapter 5, where a a more in-depth analysis of the optimal configurations will be performed based on the results from the radiation pattern analysis.

4.1.1 Radiation pattern

As explained in Chapter 1, each satellite will carry antennas to implement beamforming method. To better understand how the arrangement of satellites, and consequently the placement of antennas, influences the resulting observation beam directed towards Earth, it is possible to visually depict the distribution of electromagnetic fields (and, by extension, the power) of an antenna array in different directions. This distribution is named the radiation pattern.

Chapter 1 also explained that Cubesats are designed as receiver antennas for GNSS signals. However, antennas have a fundamental characteristic: their far-field radiation pattern and reception pattern are identical, regardless of whether they are used for transmitting or receiving [16]. This is made possible by electromagnetic reciprocity. Therefore, even though Cubesats function as receiver antennas, they can be considered as transmitters for analysis. This feature will be used to study their radiation pattern and to understand their performance.

4.1.1.1 Translational phase shift

One of the basic properties of an antenna array is that the relative displacements of the antenna elements with respect to each other introduce relative phase shifts in the radiation pattern, which can then add constructively in some directions or destructively in others. This is a direct consequence of the translational phase-shift property of Fourier transforms[1]: a translation in space or time becomes a phase shift in the Fourier domain [24].

Figure 4.1 shows the translation in space of a single antenna initially placed at the origin [21]. If the original positioned antenna is supposed to have a current density $\boldsymbol{J}(\boldsymbol{r})$, then the current density of the translated antenna will be $\boldsymbol{J}_{\boldsymbol{\rho}_o}(\boldsymbol{r}) = \boldsymbol{J}(\boldsymbol{r} - \boldsymbol{\rho}_o)$. Moreover, it has been proved in the literature that the radiation pattern of an antenna element is given by the three dimensional spatial Fourier transform of current density [22]. Therefore, the radiation pattern of the space-shifted element is calculated as follow.

---

[1] Indeed, at least for planar arrays or apertures, the radiation pattern can be linked to the Fourier transform of the source distribution.

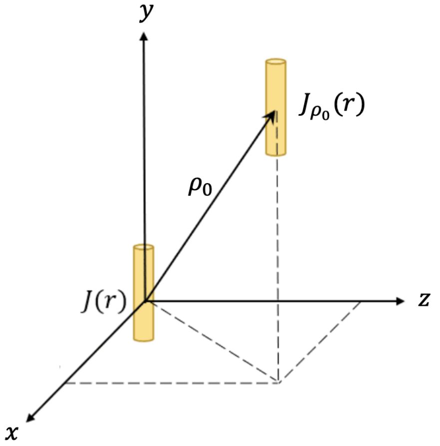

Figure 4.1: Displacement of a single antenna by a distance of ρ_o.

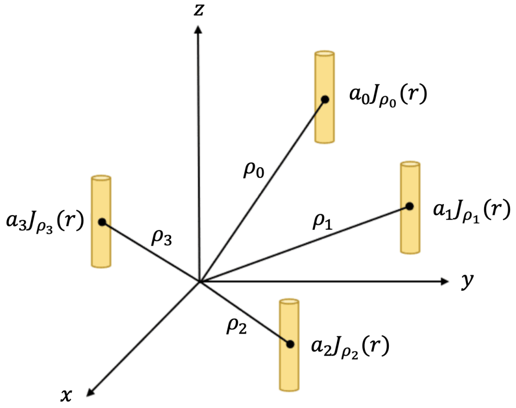

Figure 4.2: Space shift of antenna elements.

$$\begin{aligned} \boldsymbol{F}_{\boldsymbol{\rho_o}}(\hat{\boldsymbol{u}}) &= \int_V e^{jk\hat{\boldsymbol{u}}\cdot\boldsymbol{r}} \boldsymbol{J}_{\boldsymbol{\rho_o}}(\boldsymbol{r}) d^3\boldsymbol{r} \\ &= \int_V e^{jk\hat{\boldsymbol{u}}\cdot\boldsymbol{r}} \boldsymbol{J}(\boldsymbol{r}-\boldsymbol{\rho_o}) d^3\boldsymbol{r} \\ &= \int_V e^{jk\hat{\boldsymbol{u}}\cdot(\boldsymbol{r}'+\boldsymbol{\rho_o})} \boldsymbol{J}\left(\boldsymbol{r}'\right) d^3\boldsymbol{r}' \\ &= e^{jk\hat{\boldsymbol{u}}\cdot\boldsymbol{\rho_o}} \int_V e^{jk\hat{\boldsymbol{u}}\cdot\boldsymbol{r}'} \boldsymbol{J}\left(\boldsymbol{r}'\right) d^3\boldsymbol{r}' \\ &= e^{jk\hat{\boldsymbol{u}}\cdot\boldsymbol{\rho_o}} \boldsymbol{F}(\hat{\boldsymbol{u}}) \end{aligned} \tag{4.1}$$

where $\hat{\boldsymbol{u}}$ represents a vector that indicates the direction of propagation of the electromagnetic wave.

4.1.1.2 Array pattern multiplication

The following figure now depicts multiple identical single antennas positioned at various distances, ρ, from the origin. In this case, the total current density of the antenna array results in the summation of the current densities of each individual antenna element:

$$\begin{aligned} \boldsymbol{J}_{tot}(\boldsymbol{r}) &= \boldsymbol{J}_{\rho_o}(\boldsymbol{r}) + \boldsymbol{J}_{\rho_1}(\boldsymbol{r}) + ... + \boldsymbol{J}_{\rho_n}(\boldsymbol{r}) \\ &= a_0\boldsymbol{J}(\boldsymbol{r}-\boldsymbol{\rho}_o) + a_1\boldsymbol{J}(\boldsymbol{r}-\boldsymbol{\rho}_1) + ... + a_n\boldsymbol{J}(\boldsymbol{r}-\boldsymbol{\rho}_n) \end{aligned} \tag{4.2}$$

Applying the translational phase-shift property to equation 4.2, the total radiation pattern of n-elements results in:

$$\begin{aligned}\boldsymbol{F}_{tot}(\hat{\boldsymbol{u}}) &= \boldsymbol{F}_{\boldsymbol{\rho}_o}(\hat{\boldsymbol{u}}) + \boldsymbol{F}_{\boldsymbol{\rho}_1}(\hat{\boldsymbol{u}}) + ... + \boldsymbol{F}_{\boldsymbol{\rho}_n}(\hat{\boldsymbol{u}}) \\ &= a_0 e^{jk\hat{\boldsymbol{u}}\cdot\boldsymbol{\rho}_o}\boldsymbol{F}(\hat{\boldsymbol{u}}) + a_1 e^{jk\hat{\boldsymbol{u}}\cdot\boldsymbol{\rho}_1}\boldsymbol{F}(\hat{\boldsymbol{u}}) + ... + a_n e^{jk\hat{\boldsymbol{u}}\cdot\boldsymbol{\rho}_n}\boldsymbol{F}(\hat{\boldsymbol{u}}) \\ &= \boldsymbol{F}(\hat{\boldsymbol{u}})\sum_{i=0}^{n} a_i e^{jk\hat{\boldsymbol{u}}\cdot\boldsymbol{\rho}_i} \\ &= \boldsymbol{F}(\hat{\boldsymbol{u}})\boldsymbol{R}(\hat{\boldsymbol{u}})\end{aligned} \tag{4.3}$$

In this formulation, the variable $\boldsymbol{R}(\hat{\boldsymbol{u}})$ represents the array factor which takes into account both the relative translational phase shifts and the relative coefficients of the array elements [36]:

$$\begin{aligned}\boldsymbol{R}(\hat{\boldsymbol{u}}) &= \sum_{i=0}^{n} a_i e^{jk\hat{\boldsymbol{u}}\cdot\boldsymbol{\rho}_i} \\ &= \sum_{i=0}^{n} A_i \; e^{jk\hat{\boldsymbol{u}}\cdot\boldsymbol{\rho}_i} \; e^{jk\hat{u}_o\cdot\boldsymbol{\rho}_i}\end{aligned} \tag{4.4}$$

The array factor models the effect of constructive and destructive interference between the antennas in the array on the overall radiation pattern and depends on the geometry of the antenna array, the relative positions of the antennas, and their relative amplitudes and phases. The second exponential depends on $\hat{u}_o$ which correspond to the direction of observation. This is used to steer the radiated power towards a particular direction of interest (here, the specular point) by simply adjusting the relative phases of the array elements.

The factor $\boldsymbol{F}(\hat{\boldsymbol{u}})$ represents the individual radiation element of each antenna in the array. To determine its value, it is necessary to understand the radiation pattern of each individual antenna element on the Cubesat, known as the element pattern. Indeed, unlike a single antenna, a Cubesat is equipped with multiple antennas [29]. By combining the radiation patterns of these antennas, a composite element pattern can be determined for the entire CubeSat. Particularly, this composite element pattern exhibits wide radiation coverage in the direction of observation. As a consequence, the composite element pattern can be approximated using the pattern of an isotropic antenna in the direction of observation. An isotropic antenna is a theoretical antenna that uniformly radiates and receives electromagnetic waves in all directions. Thus, $\boldsymbol{F}(\hat{\boldsymbol{u}})$ equals 1 when $\hat{\boldsymbol{u}}$ is directed towards the glistening zone. In other words, it will be considered that the radiation pattern of the antenna array will only depend on its array factor in the direction of observation.

4.1.2 Ground resolution and glistening zone

The ground resolution in this project must not exceed 1 kilometer, which requires to maintain a sufficiently narrow beamwidth. The beamwidth is commonly quantified using the half-power beamwidth (HPBW). The HPBW denotes the angular span over which the radiated power of the antenna array decreases by 50% (equivalent to -3 dB on the radiation pattern) from the peak of the main beam [18] [8]. Hence, to determine the HPBW, the angular separation, α, at 3 dB below the peak is measured (cfr. Figure 4.3a).

Then, Figure 4.3b provides a schematic visualization of how the angular distance is related to the ground resolution. However, under the assumption of small angles, a linear approximation can be employed to derive the following resolution formula:

$$R = d_{CE} \cdot \tan(\alpha) \tag{4.5}$$

Here, d_{CE} represents the radial distance that separates the Cubesats swarm from the surface of the Earth, which is 400 km.

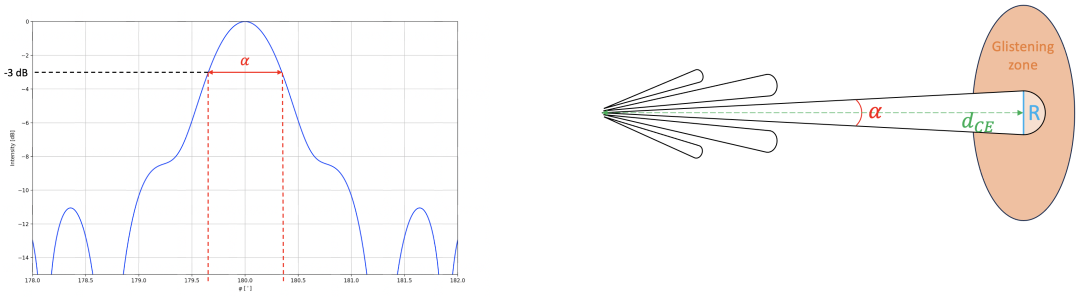

(a) Half-Power BeamWidth

(b) Resolution computation

Figure 4.3: (a) α is calculated on the radiation pattern, and (b) connect it to ground resolution through depiction of emission lobes from the CubeSats swarm on the Earth's surface.

Equation 4.5 will also be used to determine the size of the glistening zone (cfr. Section 1.3), thus enabling a graphical evaluation of whether the constraint regarding the height of the secondary lobes in a specific region is indeed satisfied.

4.1.3 Ground spot

The concept of ground spots involves projecting the power distribution radiated by an antenna array onto the Earth's surface, thereby creating regions of signal illumination. These ground spots represent the measurement on the Earth's surface of the illumination caused by the GNSS signal emitted and received by the Cubesats swarm. This allows for a graphical and geographical visualization of the array factor on the Earth's surface, aiding in understanding the directional characteristics of an antenna array in various spatial directions.

The methodology employed for computing ground spots follows a similar approach to the one used for calculating the overall array factor across the entire sphere (as discussed in Section 4.1.1). However, in this case, the focus shifts towards computing the array factor for a specific area surrounding the specular point. As depicted in Figure 4.4, a virtual grid is established within this specific zone. The axes of the contour plot are represented in meters, depicting the ground illumination over an area of 10 square kilometers. For each intersection point on this grid, the array factor is computed for the corresponding direction vector denoted as $\hat{\boldsymbol{u}}$. Additionally, the array factor calculation takes into consideration the direction of $\hat{\boldsymbol{u}}_{\mathbf{0}}$, which indicates the specular point's position. Referring to equation 4.3 it becomes evident that $\hat{\boldsymbol{u}}_{\mathbf{0}}$ appears in the second exponential term of the array factor, allowing the main lobe to be directed towards the desired direction, which in this case is the specular point. Finally, the finer the grid, the more values of $\hat{\boldsymbol{u}}$ can be computed, resulting in a more precise representation of the illumination.

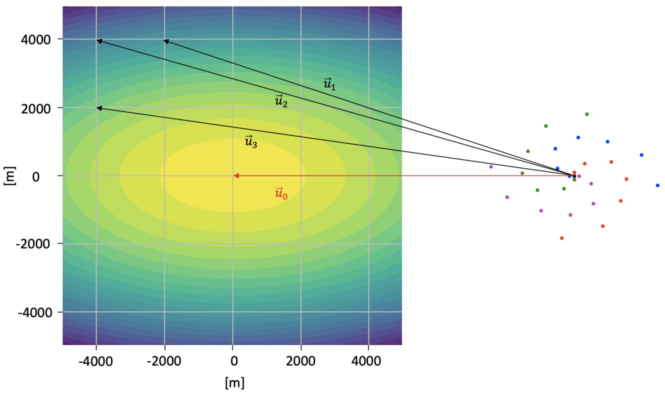

Figure 4.4: Principle of the ground spot computation

4.2 Analysis stage

The analysis phase serves as a sort of pre-selection process. Its purpose is to calculate the radiation pattern for each configuration to determine which ones yield satisfactory results based on the project requirements. As a reminder, the objective is to achieve beamwidth with a resolution of less than 1 km, while simultaneously maintaining secondary lobes below -10 dB in the glistening zone. It is well-known that a trade-off exists between resolution and the size of secondary lobes [6]. Thus, the idea is to identify the configurations that offer the best trade-off.

4.2.1 Geographic system of coordinates

Before analyzing the different antenna configurations, it is necessary to establish a reference frame to describe the direction of radiation in the antenna's radiation pattern. The spherical system of coordinates in accordance with geographical conventions has been selected [37].

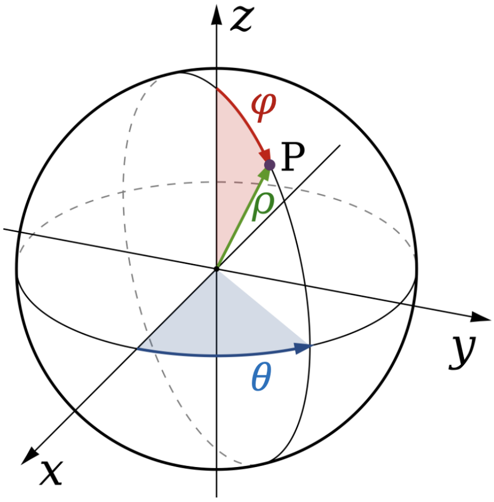

Figure 4.5: Spherical coordinate system

The conventions of this system, which will be used in the following stages of analysis, are:

- ρ: distance from the point P to the centre of the reference frame
- θ: longitude, measured from the x-axis ($-\pi \leq \theta \leq \pi$)
- φ: colatitude, measured from the z-axis ($0 \leq \varphi \leq \pi$)

Following the relative system of coordinates defined by the (x, y, z) axes in Chapter 2, the conversion from spherical to Cartesian coordinates occurs as follows:

$$\begin{cases} x = \rho \sin\varphi \cos\theta \\ y = \rho \sin\varphi \sin\theta \\ z = \rho \cos\varphi \end{cases} \tag{4.6}$$

where the proper selection of θ and φ is important to highlight the main lobe in the radiation patterns cross-sections.

4.2.2 Comparison between formations

As previously observed, antenna networks are asymmetrical, which directly impacts the radiation pattern, resulting in a lack of symmetry. Hence, in this section, the 2D cuts proposed along θ or φ will only serve as a preliminary step in selecting the best configurations based on the emerging trends. A more detailed analysis of the optimal antenna configurations will be conducted in Chapter 5 using contour plots.

The comparison will be based on the array factor for each configuration, which is visualized using a decibel scale. The following figures represent selected portions of the radiation pattern that highlight the main beam. To provide a clearer representation of the beamwidth, the angular scale on the x-axis has been converted into kilometers. Additionally, the glistening zone has been delineated to define the boundary where the height of the sidelobes becomes significant.

The following results represent the best outcomes achieved for each configuration. Taking into account the general shape of the different antenna formations, these configurations were defined based on a little optimization algorithm to determine the ideal set of eight initial conditions (cfr. Section 2.3) that defines the position of each antenna.

4.2.2.1 Single Orbit Formation

The single orbit formation provides a resolution of 0.89 km while the secondary lobes are maintained under -4.5 dB. Despite a reglementary distance between antennas, the sidelobes can not be maintained at an acceptable level.

4.2.2.2 Symmetrical Orbit Formation

The symmetrical orbit formation provides a resolution of 0.56 km while the secondary lobes are maintained under -5.5 dB. The resolution is significantly better

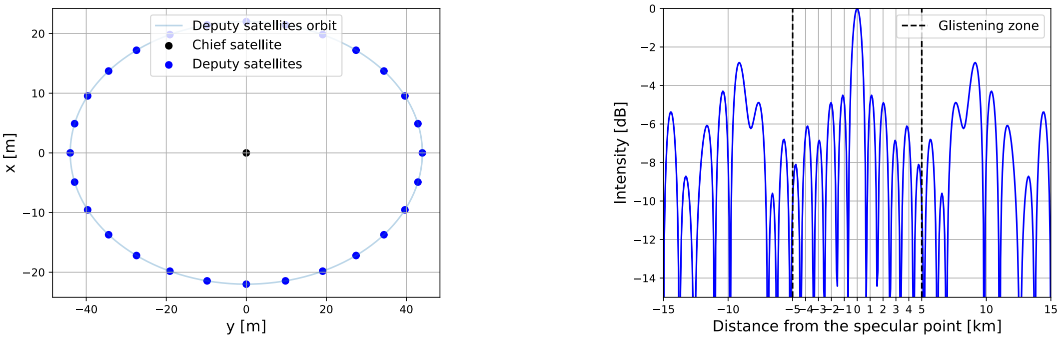

Figure 4.6: Radiation pattern of the optimal single orbit constellation composed of 29 satellites in the x-y plane, resulting in a beamwidth of 0.89 km.

compared to other formations, thanks to its extended apparent length. Taking into account the trade-off between beamwidth and sidelobe size, since the resolution is improved, the secondary lobes cannot be maintained at a sufficiently low level.

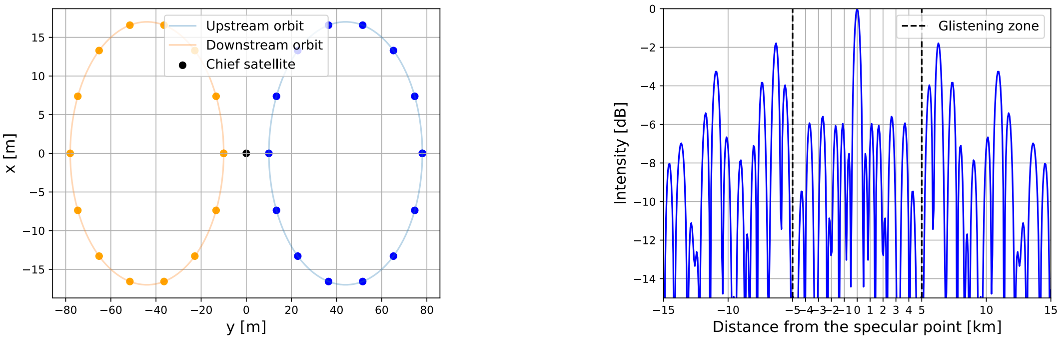

Figure 4.7: Radiation pattern of the optimal symmetrical orbit constellation composed of 29 satellites in the x-y plane, resulting in a beamwidth of 0.56 km.

4.2.2.3 Spiral Formation

The analysis of various spiral configurations highlights the dependence of the beamwidth on the radius of the formation. Specifically, for configurations with similar number of antenna, the variation in the number of arms has a small impact on the ground resolution, which remains within the same order of magnitude for approximately identical spiral radii.

2-arms spiral

The spiral configuration with 2 arms provides a resolution of 1.07 km while the secondary lobes are maintained under -8.5 dB. Again, the minimal distance of 2 m between antennas adheres to the constraint but the sidelobes remain too high in the glistening zone. However, it is worth noting the improvement in results compared to the previous formations.

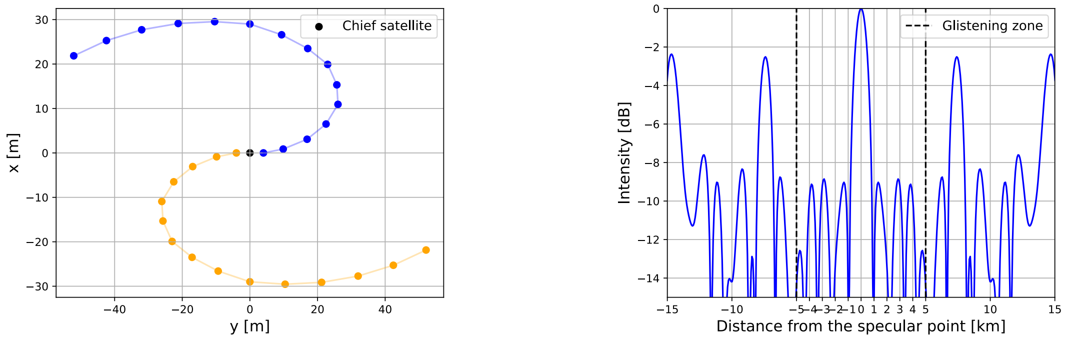

Figure 4.8: Radiation pattern of the optimal 2-arms spiral constellation composed of 31 satellites in the x-y plane, resulting in a beamwidth of 1.07 km.

3-arms spiral

The spiral configuration with 3 arms provides a resolution of 0.88 km while the secondary lobes are maintained under -8.5 dB.

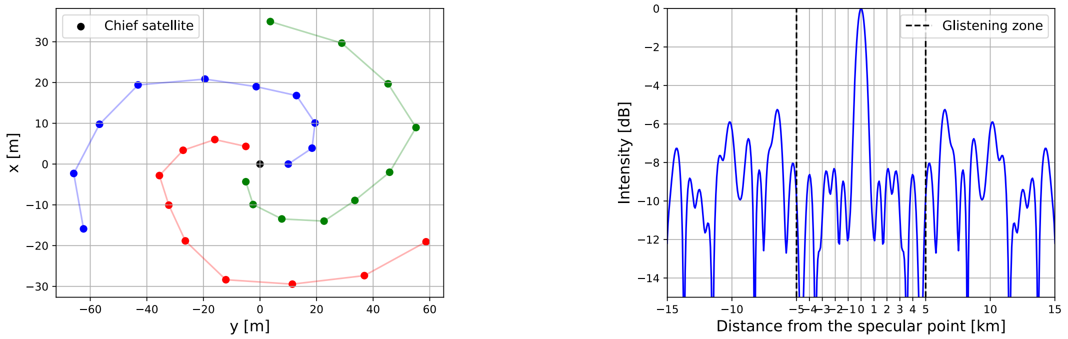

Figure 4.9: Radiation pattern of the optimal 3-arms spiral constellation composed of 31 satellites in the x-y plane, resulting in a beamwidth of 0.88 km.

4-arms spiral

The spiral configuration with 4 arms provides a resolution of 0.94 km while the secondary lobes are maintained under -12.5 dB. By ensuring a minimum distance of 4 meters between two antennas, this configuration meets all the specified constraints.

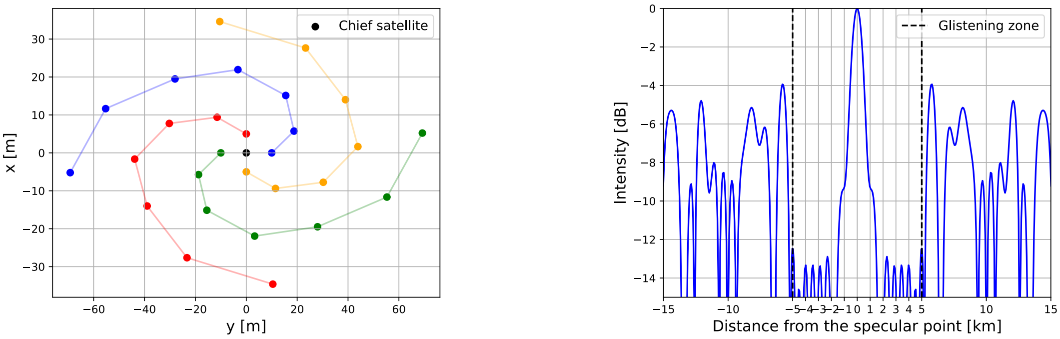

Figure 4.10: Radiation pattern of the optimal 4-arms spiral constellation composed of 29 satellites in the x-y plane, resulting in a beamwidth of 0.94 km.

5-arms spiral

The spiral configuration with 5 arms provides a resolution of 1.08 km while the secondary lobes are maintained under -9 dB.

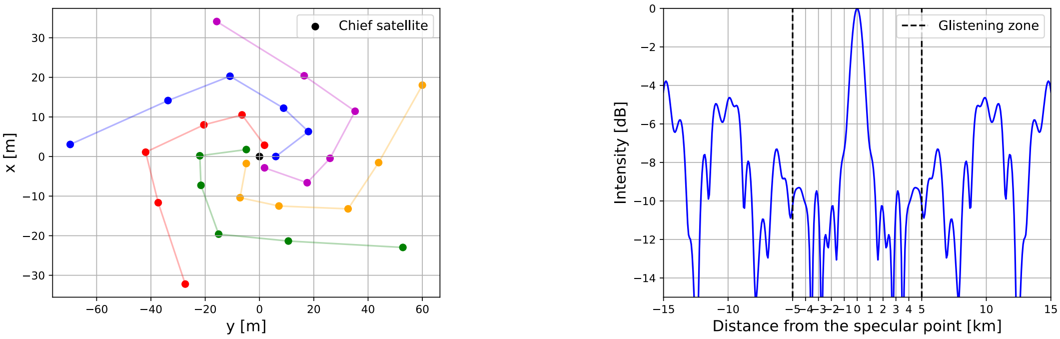

Figure 4.11: Radiation pattern of the optimal 5-arms spiral constellation composed of 31 satellites in the x-y plane, resulting in a beamwidth of 1.08 km.

4.2.2.4 Y-shaped Formation

The Y-shaped configuration provides a resolution of 0.99 km while the main secondary lobes are maintained under -9 dB and intensively decrease away from the main lobe.

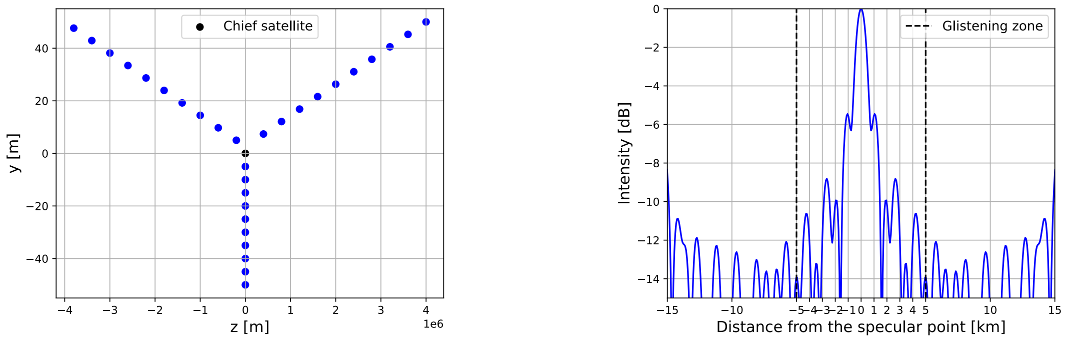

Figure 4.12: Radiation pattern of the optimal Y-shaped constellation composed of 31 satellites in the z-y plane, resulting in a beamwidth of 0.99 km.

Chapter 5

Results and Discussion

In this section, the evolution of ground illumination caused by signal reflection will be discussed. The focus is on defining the factors influencing this illumination and attempting to understand its evolution. By examining these aspects, insights can be gained into the complex dynamics that govern ground illumination and its correlation with Cubesats formations.

5.1 Ground spot evolution

As already mentioned, ground spots provide valuable insights into signal illumination taking place on the Earth's surface. These ground spots are influenced by a multitude of factors, such as the type of formation flight, the number of satellites within a constellation, the inclination of the satellite plane, the position of the GNSS satellite and the non-fixed nature of the formations. This section aims to delve into the influence of these factors on shaping ground spot characteristics.

In the course of Earth observation, maintaining isotropic resolution is important, which means that for a given configuration, it is desirable to have a relatively circular beam. The analysis of ground spots that follows will be based on the criterion of the axial ratio[1] of the main beam. In this context, the axial ratio represents the ratio between the length and width of the main beam. However, no specific rule has been established yet to determine the axial ratio threshold beyond which the ground resolution becomes too anisotropic to yield reliable results. In this study, a somewhat arbitrary limit of an axial ratio of 2 has been considered. Beyond this threshold, the resolution is deemed to be anisotropic.

---

[1] Here, the term "axial ratio" does not pertain to polarization characteristics.

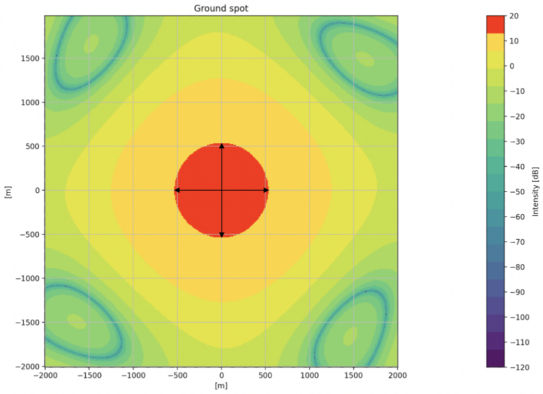

Figure 5.1: Representation of a ground spot with an axial ratio equal to 1, indicated by the equal lengths of the black arrows on the main beam spot. This implies a perfectly isotropic resolution.

5.1.1 Influence of type of formation

Based on what has been demonstrated in the previous analysis section, Y-shaped, and spiral configurations appear to be the most promising. The difficulty in examining radiation pattern cuts, as illustrated previously, arises from the lack of symmetry in the satellite formation. This results in an anisotropic radiation pattern and, consequently, an anisotropic ground spot. While the cut may appear interesting in 2D, the ground spot enables effective visualization and extraction of which configuration seems most suitable.

As it is demonstrated on Figure 5.2, the Y-shaped satellite configuration finally appear not suitable for Earth observation due to its inherent limitations. While this configuration can provide convincing results with isotropic ground resolution, the problem lies in its evolution over time. Over an orbital period, the Y-shaped configuration inevitably passes through two positions where the arms are aligned, forming a straight line formation tangent to the orbital plane. These significant changes in the configuration shape have a strong impact on the ground spot, making it impossible to maintain isotropy with an axial ratio below 2 over a complete orbital period (cfr. Figure 5.2b).

However, it is worth noting the practicality of Y-shaped configurations for specialized missions that target the observation of specific areas on Earth. Given their high ground resolution and low sidelobes when fully deployed, they could be highly effective for achieving very focused and specific objectives. Hence, the variation of the ground spot beyond this observation zone becomes inconsequential.

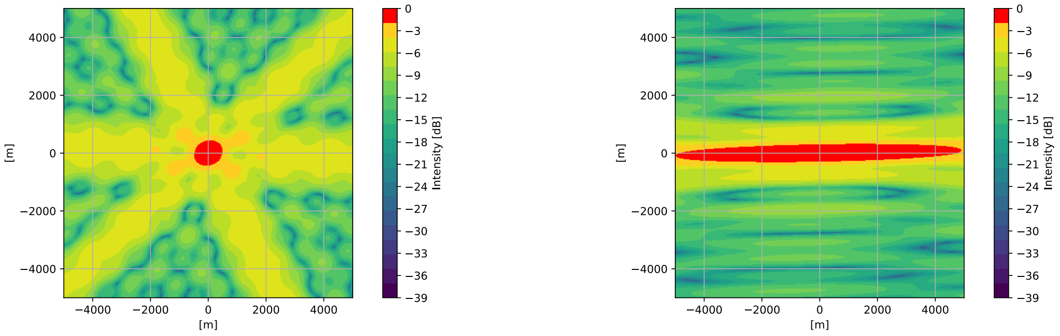

(a) Position of 29 Y-shaped Cubesats swarm: half an orbital period

(b) Position of 29 Y-shaped Cubesats swarm: 3/4 of the orbital period

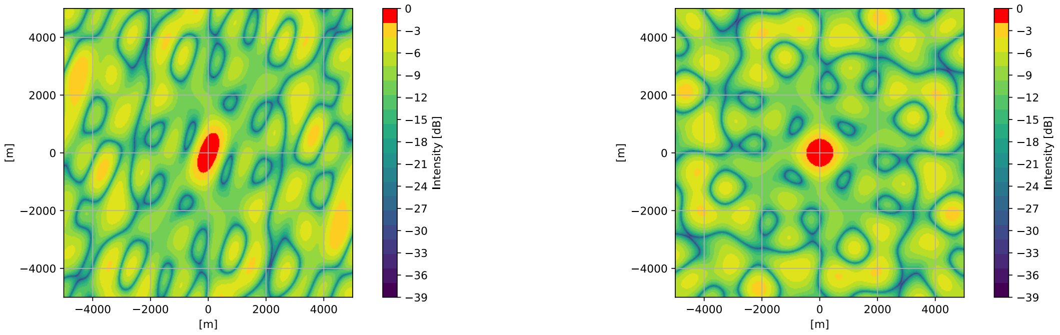

(c) Position of 29 spiral-shaped Cubesats swarm: half an orbital period

(d) Position of 29 spiral-shaped Cubesats swarm: 3/4 of the orbital period

Figure 5.2: Evolution of ground spots along the circular orbit

On the other hand, the spiral configuration developed in 4.2.2.3 is capable of maintaining a relatively constant shape. Furthermore, as it will be studied in the following sections, variations in the configuration due to orbital dynamics can be balanced by an inclination along the z-axis. This highlights the limitation of the Y arrangement, which is fixed in the y-z plane.

The spiral formation ultimately appears to be the most suitable for achieving the objectives of this project. Therefore, the subsequent analyses will be based on this precise configuration with 29 satellites.

5.1.2 Influence of formation density

One interesting finding relates to the number of satellites that make up the constellation. As demonstrated by the following figures, while maintaining the same outer radius of a spiral formation, reducing the density of satellites per arms significantly reduces the ground resolution.

Indeed, while a distinct main lobe can be observed in a configuration with 29 satellites, the configuration with fewer satellites reveals numerous secondary lobes, reaching a height similar to that of the main beam, in the vicinity of the specular point. These sidelobes will therefore interfere with signal reception, inevitably resulting in a lack of accuracy in the extracted data.

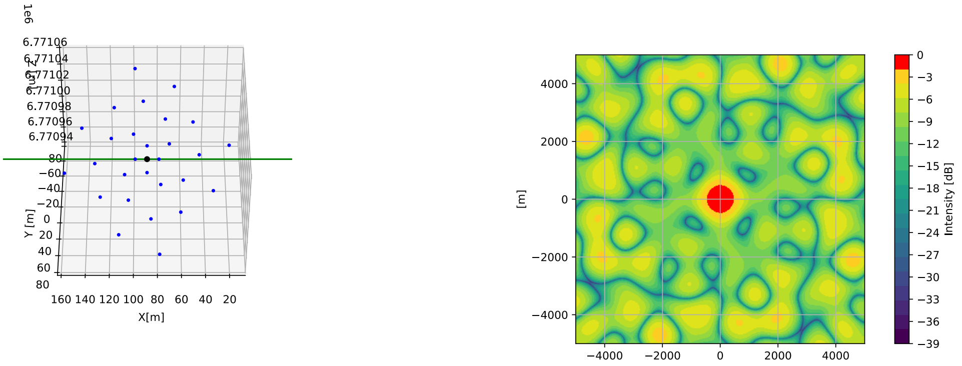

(a) Spiral formation: 29 satellites on 4 arms

(b) Ground resolution

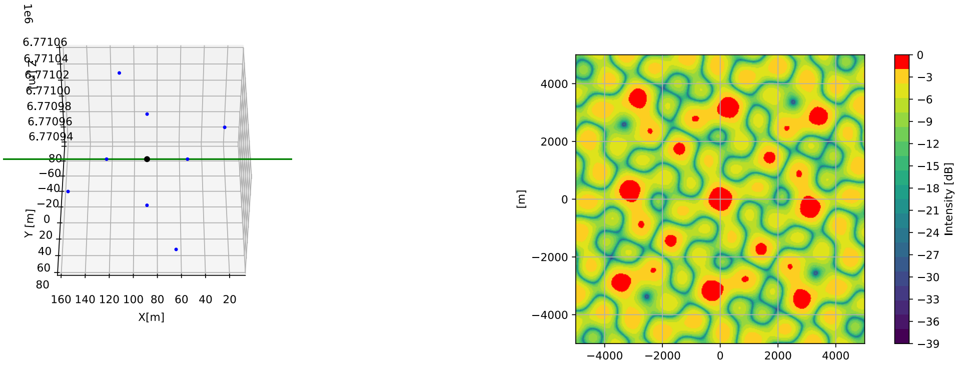

(c) Spiral formation: 9 satellites on 4 arms

(d) Ground resolution

Figure 5.3: Comparison of spiral density and corresponding ground spots.

5.1.3 Influence of formations tilt

In Section 3.1.1.4, the demonstration of the inability to keep the Cubesats' plane locally parallel to the Earth's surface emphasizes a critical dynamic constraint. The aim of this section is to underline this constraint by investigating the influence of the satellite plane tilt on the ground spot morphology.

The following analysis is conducted at a specific (and arbitrary) orbital time to ensure that the satellite formation, the position of the GNSS satellite, and consequently, the specular point remains fixed. The analyzed satellite configuration is the spiral one, studied 4.2.2.3. The Cubesats' orbit remains a polar orbit, inclined 90 degrees to the equatorial plane at an altitude of 400 km. The GNSS orbit follows the path of the Galileo satellites, inclined at 56° with an altitude of 23222 km. The time considered in this analysis positioned the system at three-quarters of the orbital period, meaning that the Cubesats swarm is located above the North Pole at this particular moment. A schematic of the system is depicted in Figure 5.4.

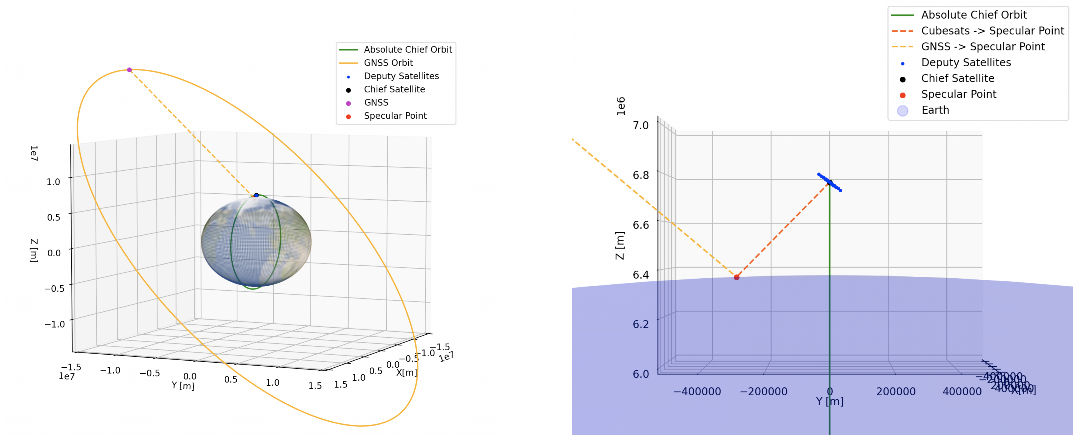

(a) General system of analysis

(b) Close-up view of the analyzed system

Figure 5.4: Illustration of the system to understand the impact of the Cubesats' plane inclination for a fixed GNSS satellite position.

A first configuration is tested in Figure 5.5c by tilting the satellite plane at 112° relative to the radial axis (equivalent to 10° relative to the plane locally parallel to the Earth's surface). This initial setup demonstrates that the main beam can indeed appear fully circular, even when constrained by the inclination of the satellite's plane. The additional configurations 5.5a and 5.5e provide clearer insights into the intricate dynamics governing the ground spot. As demonstrated in Section 3.1.1.4, tilting the satellite plane inevitably causes the Cubesats' formation to stretch along its minor axis while maintaining the major axis unchanged. This effect is visible in Figures 5.5b and 5.5f, where the elongation and compression of the satellite formations directly impact the ground illumination. An inverse correlation becomes evident: when the configuration elongates along a certain axis, the ground illumination compresses along the same axis, and vice versa.

For this specific configuration, formations presented in 5.5a and 5.5e represent the limits beyond which ground resolution is no longer sufficiently isotropic. Therefore, it can be concluded that within a range of satellite plane inclination from 100.3° to 140.2° relative to the radial axis connecting to the Earth's center, the axial ratio of the ground spot remains below 2. This wide range of inclinations where the resolution remains isotropic offers a significant advantage in mitigating technical failures and precision errors in satellite plane inclination.

Hence, this initial analysis aims to demonstrate how the ground spot's characteristics are influenced by the orbital constraint of the satellite plane's tilt. This highlighted the inverse relationship between the stretching of satellite formations and shape of the main beam. Nevertheless, it can be observed that, for a specific stretching, and consequently tilt, depending on the GNSS satellite position, it remains feasible to maintain a circular ground spot, ensuring isotropic resolution (cfr. Figures 5.5c et 5.5d).

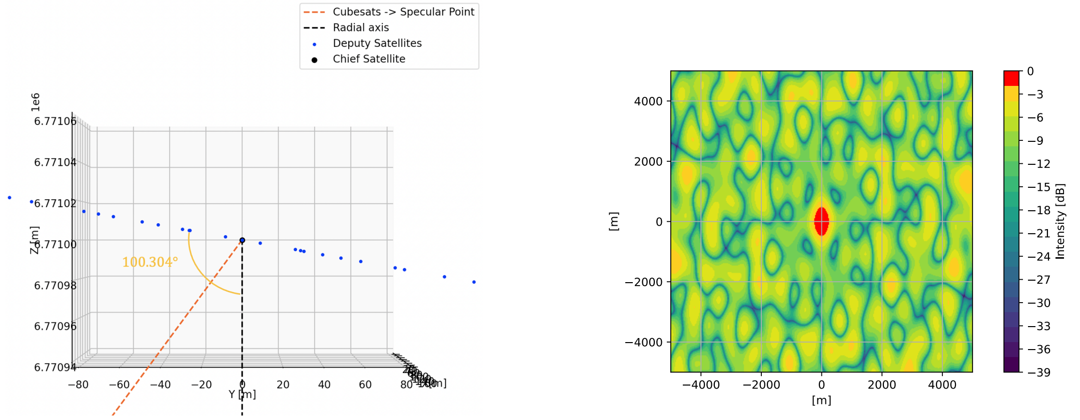

(a) Inclination of 100.304° above the radial axis achieve by setting $z_0 = 5.5x_0$

(b) Limit of the axial ratio: the vertical axis appears twice as long as the horizontal one.

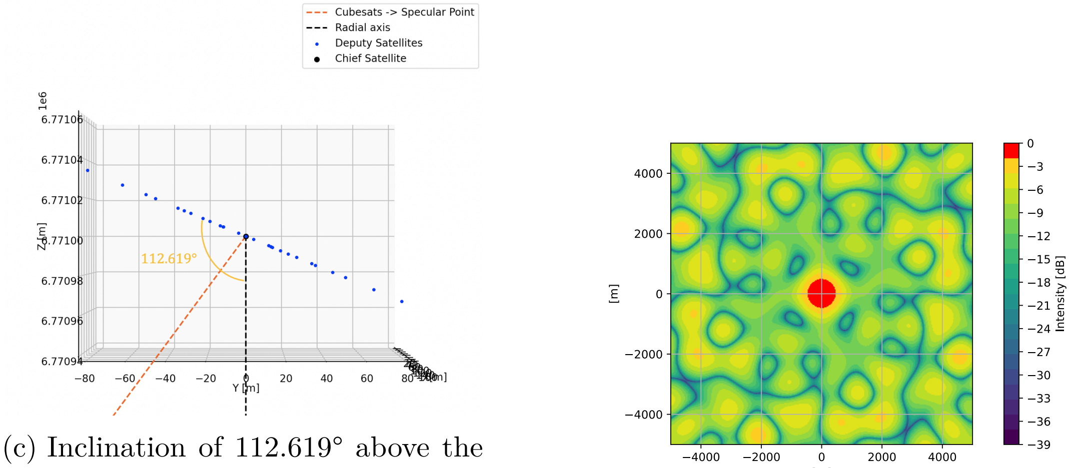

(c) Inclination of 112.619° above the radial axis achieve by setting $z_0 = 2.4x_0$

(d) Axial ratio = 1

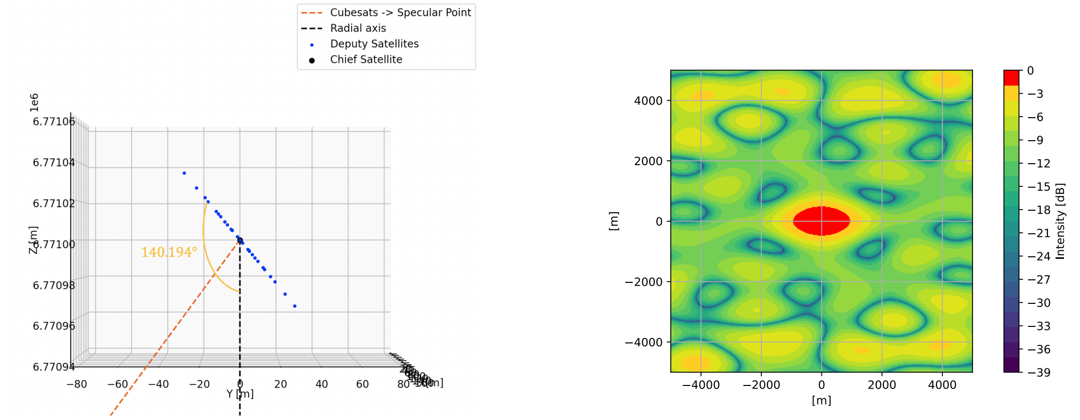

(e) Inclination of 140.194° above the radial axis achieve by setting $z_0 = x_0/1.2$

(f) Limit of the axial ratio: the horizontal axis appears twice as long as the horizontal one.

Figure 5.5: Evolution of the ground resolution with the Cubesats swarm inclination

5.1.4 Influence of GNSS satellite

The previous analysis explored the influence of the satellite plane's tilt on the ground illumination by considering the position of the GNSS satellite and, consequently, the specular point fixed. This section delves into examining the impact of the GNSS satellite's position on the ground spot for a fixed Cubesat configuration. A subsequent study will be conducted to determine whether the tilt of the Cubesats' plane can compensate for the GNSS satellite's position to result in a ground spot that remains sufficiently circular.

5.1.4.1 Position of the GNSS satellite

The investigation begins by analyzing how the GNSS satellite's position within the formation plane's horizon impacts the ground spot. Following the favourable results obtained with a satellite plane inclination of 112.6° relative to the radial axis, this configuration 5.5c serves as a baseline. Indeed, as it produced a completely isotropic ground spot, the formation is used to investigate how variations in the position of the GNSS satellite, and hence the position of the specular point, affect the ground spot morphology. This analysis aims to provide an estimate of the range of motion that the GNSS satellite can traverse for a fixed Cubesat configuration, before yielding less convincing outcomes.

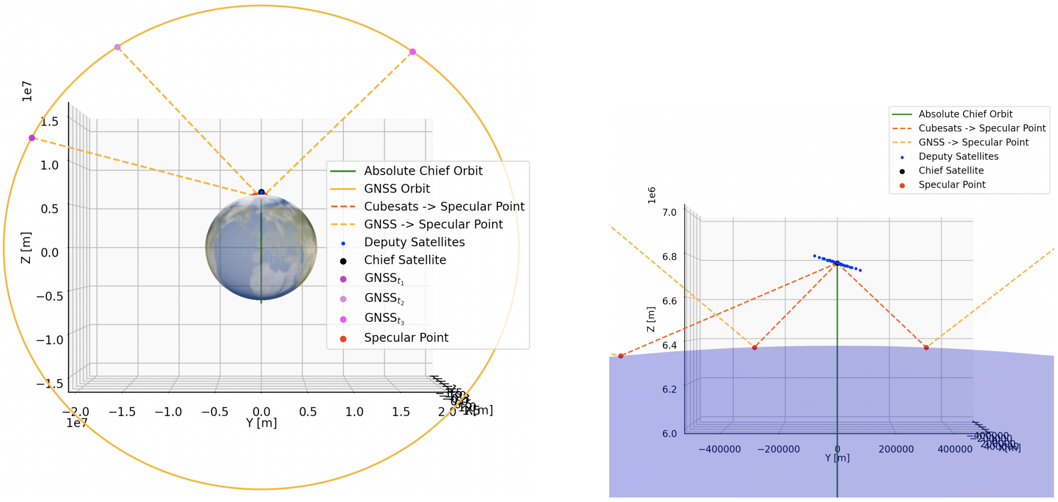

(a) General system showing the 3 positions of the GNSS satellite

(b) Close-up view showing the 3 specular points

Figure 5.6: Illustration of the system to understand the influence of the GNSS satellite's position relative to a fixed Cubesat swarm.

To conduct this type of analysis, a fictitious orbit is used to position the GNSS satellites in a relevant manner. The GNSS orbit remains unchanged in terms of its orbital parameters, but it is now configured to be inclined at 90 degrees, creating a polar orbit, while the right ascension of the ascending node is set to 90 degrees as well. By maintaining the Cubesats on the same circular orbit, this configuration ensures that the two orbits are in perpendicular planes. Then, while maintaining the fixed position of the Cubesats' formation, the GNSS position can be adjusted to identify the precise location within the swarm's horizon that produces a circular ground spot. To achieve this, three different positions of the GNSS satellite are considered and represented in Figure 5.6.

As the focus shifted to examining the influence of the GNSS satellite's position, it is pertinent to characterize configuration 5.5c based on the angle between the Cubesats' plane horizon and the line connecting the formation to the GNSS satellite. Figure 5.7c illustrates this scenario, indicating that for a configuration inclined by 112° relative to the radial axis, the GNSS satellite is positioned 47° above the satellite plane's horizon to achieve an axial ratio of 1 (cfr. Figure 5.7d). Starting from this position, the GNSS satellite's movement along its orbit is considered to evaluate the effects on this initially circular ground spot. In this way, the limits of the GNSS satellite positioning giving rise to an anisotropic resolution, i.e. an axial ratio equal to 2, can be determined. These limits are represented in Figures 5.7a and 5.7e. Hence, it can be observed that the GNSS satellite can move from 14° to 135° relative to the horizon of the satellite configuration while maintaining a sufficiently isotropic ground resolution. This illustrates that without altering the configuration and position of Cubesats, ground resolution can be maintained sufficiently isotropic despite significant variations in the GNSS positions.

5.1.4.2 Balance through formation tilt

The second stage of this analysis aims to ascertain whether the GNSS satellite's positioning can be balanced by modifying the tilt of the Cubesats's plane to achieve isotropic resolution. Given the promising outcomes depicted in Figure 5.7d for a specific GNSS satellite position and Cubesats's configuration, it is pertinent to determine if similar results can be achieved for variations in the specular point's position.

By adopting the same arrangements as shown in Figures 5.7a and 5.7e, the variation of the satellite plane's tilt is explored to assess its impact on ground illumination. The outcomes in Figures 5.8a and 5.8c demonstrate that adjusting the inclination of the Cubesats' plane can transform a configuration that initially resulted in an axial ratio of 2 into one that yields an isotropic main beam. As a result, a noteworthy conclusion can be derived from this analysis: the positions of

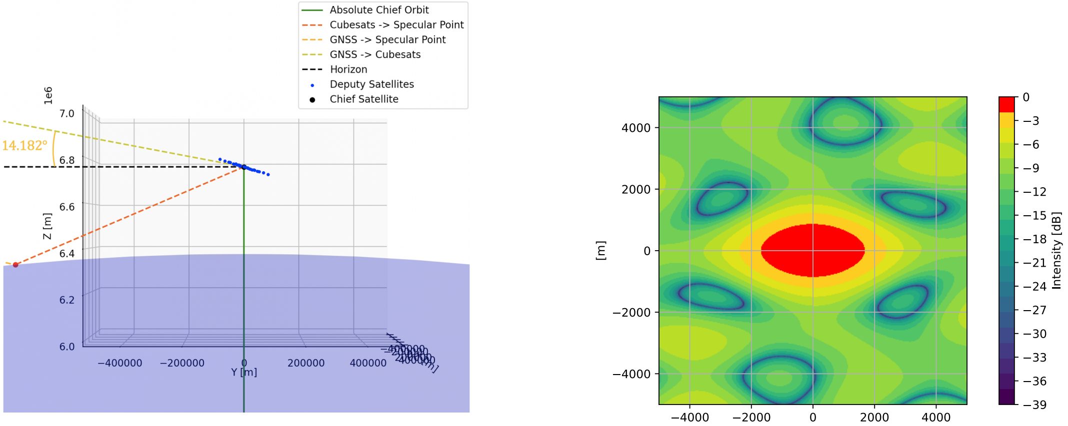

(a) GNSS$_{t_1}$ satellite position: 14.182° above the Cubesats horizon

(b) Left boundary: axial ratio = 2

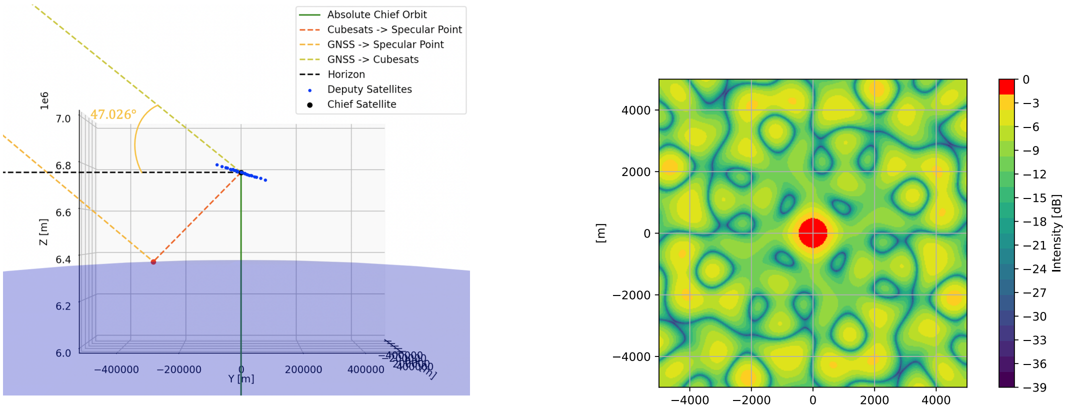

(c) GNSS$_{t_2}$ satellite position: 47.026° above the Cubesats horizon

(d) Benchmark ground spot

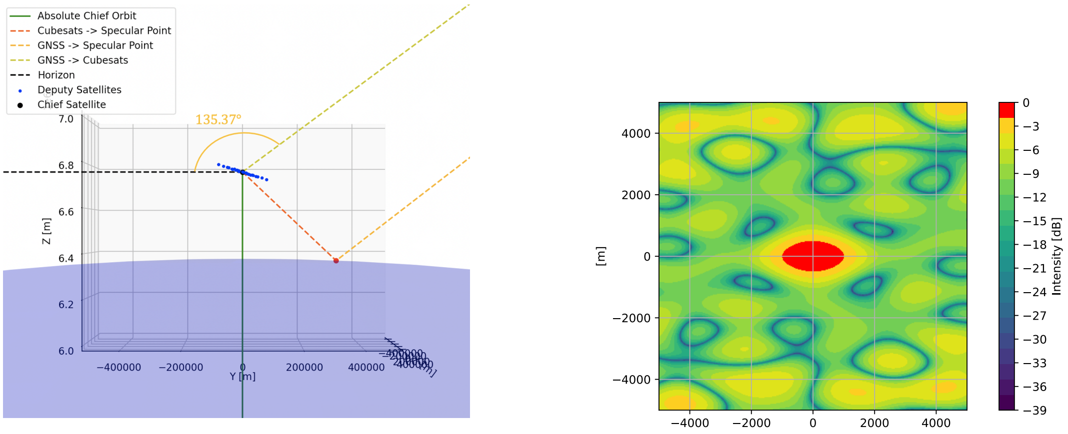

(e) GNSS$_{t_3}$ satellite position: 135.37° above the Cubesats horizon

(f) Right boundary: axial ratio = 2

Figure 5.7: Evolution of the ground resolution with the position of the GNSS satellite

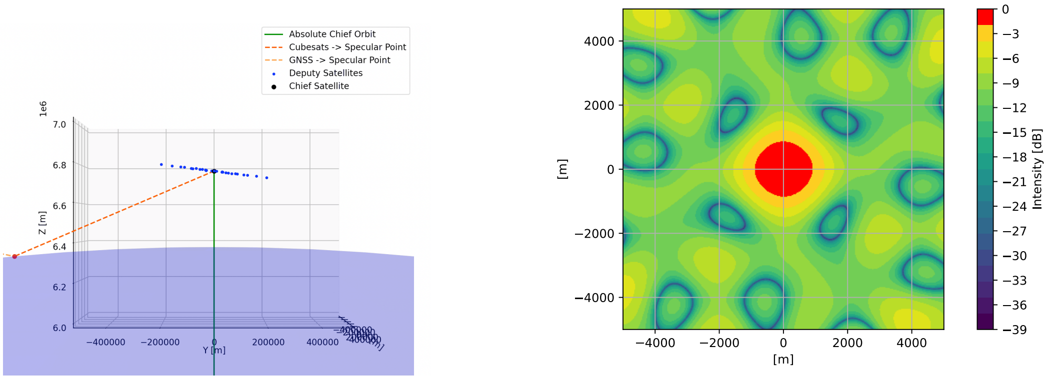

(a) GNSS$_{t_1}$ for $z_0 = 6x_0$ (b) Axial ratio = 1

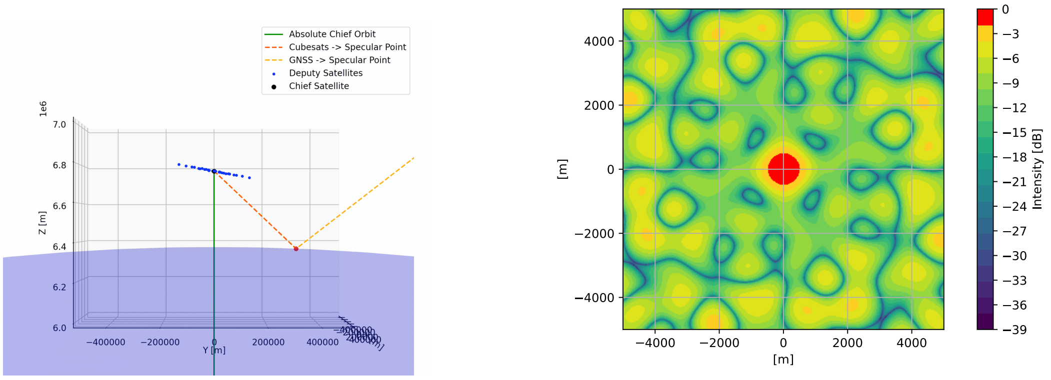

(c) GNSS$_{t_3}$ for $z_0 = 4x_0$ (d) Axial ratio = 1

Figure 5.8: Illustration of the positions of the GNSS$_{t_1}$ and GNSS$_{t_3}$ with variation in the Cubesats swarm tilt, resulting in isotropic resolution.

the GNSS satellite within the Cubesat formation's horizon can be counterbalanced by adjusting the formation plane's tilt, leading to isotropic resolution and an axial ratio equal to 1.

However, the angle between the radial axis connecting the Cubesat formation to the Earth's center and the axis linking this formation to the specular point will impact the resolution. Indeed, it is observed in Figure 5.8a, where this angle is sufficiently large, that the satellite configuration must significantly elongate to maintain circular resolution, thus increasing the radius of the mainbeam.

5.1.5 Temporal evolution

As discussed in Chapter 1, a significant consideration for Earth observation using an antenna array mounted on Cubesats is the orbital constraint associated with the non-static nature of a formation during its temporal evolution. Indeed, given that the deputy satellites circulate along elliptical (and not circular) relative orbits around the chief satellite (cfr. Section 3.1.2.3), this inevitably results in variations in the configuration's arrangement. These variations in the antenna array's shape directly influence the morphology of the ground spot. Therefore, having examined the behaviors of configurations within a specific temporal context, it becomes pertinent to explore how the evolution of these configurations over time affect the ground illumination.

To this end, the orbital parameters of the GNSS and Cubesat orbits are once again considered as in Section 5.1.3. The two satellites are placed on separate orbits, and in this analysis, they are launched simultaneously, ensuring that they remain in continuous line-of-sight with each other. The configurations are computed for arbitrary positions at 1/5, 3/5, and 4/5 of the orbital period and can be seen in Figure 5.9.

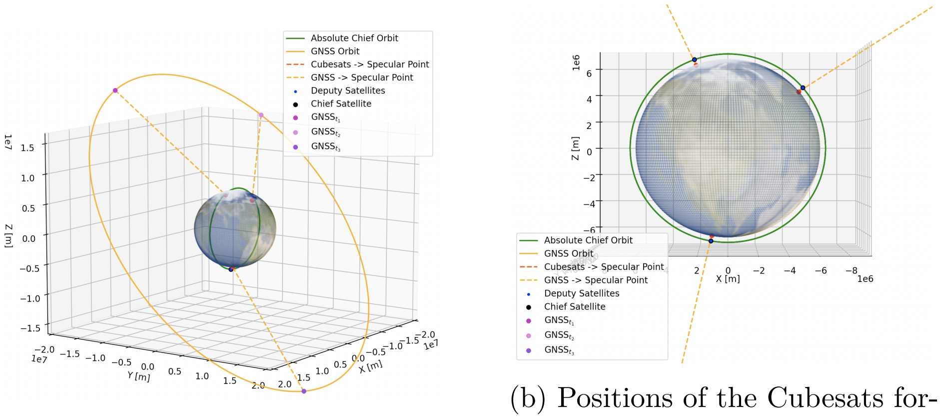

(a) General system of analysis

(b) Positions of the Cubesats formations around the Earth

Figure 5.9: Illustration of the system to understand the influence of the non-static nature of the Cubesats' formations.

As demonstrated by the graphs in Figure 5.10, the evolution of the formation over time can once again be counterbalanced by the inclination of the satellite plane. Thus, for any position of the GNSS and the Cubesats' plane around Earth, the electromagnetic beam directed towards the Earth's surface can consistently provide isotropic resolution, with an axial ratio close to 1.

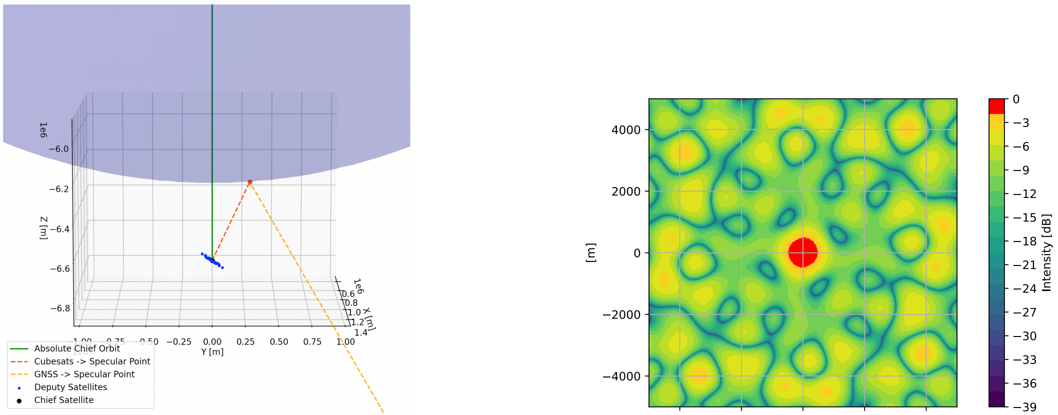

(a) 1/5 of the orbital period: $z_0 = 2.3x_0$ and $\theta_0 = 65°$

(b) Axial ratio = 1

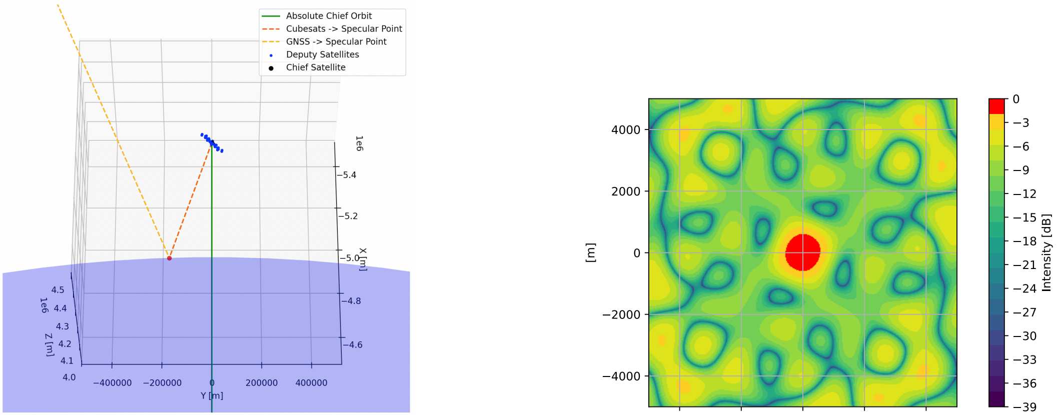

(c) 3/5 of the orbital period: $z_0 = 1.3x_0$ and $\theta_0 = 70°$

(d) Axial ratio = 1

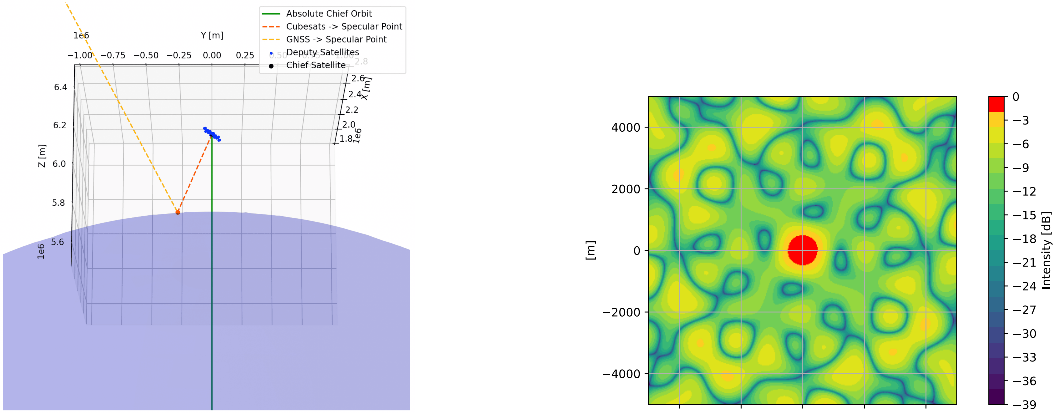

(e) 4/5 of the orbital period: $z_0 = 2.1x_0$ and $\theta_0 = 105°$

(f) Axial ratio = 1

Figure 5.10: Temporal evolution of ground resolution with variation in GNSS satellite position and Cubesats Swarm inclination.

Conclusion

Utilizing a network of antennas mounted on miniature satellites to enable high-resolution Earth observation while minimizing mission costs presents a formidable technological challenge. This ambitious project is still in its early stages, with many challenges yet to be explored before its realization. This thesis aims to contribute to this innovative endeavor, which could potentially mark a turning point in the history of space-based Earth monitoring.

The primary goal of this work is to determine the optimal Cubesat formation for achieving high-precision Earth observation. To accomplish this, the thesis is structured around four main axes.

Firstly, a contextual foundation was established, explaining the Earth observation method through reflectometry (GNSS-R) and justifying the selection of Cubesats as antenna carriers within this bi-static radar context, emphasizing their advantages of ease of deployment and cost-effectiveness. The following section delved into identifying constraints and challenges related to orbital mechanics, highlighting the difficulty of flying a Cubesat swarm in space while avoiding collisions. With the objective of replicating the behavior of a large continuous aperture antenna, the targets for ground resolution and sidelobes within the glistening zone were also discussed.

A review of existing literature was then conducted to derive the Clohessy-Wiltshire equations, which describe the relative motion of secondary satellites around a lead satellite and provide the foundation for the entire project. This study highlighted various mechanical challenges involved in this mission, such as the inability to maintain a spiral formation locally parallel to the Earth's surface and the difference in angular velocities among satellites leading to non-fixed formations over time. In addition, a section has been devoted to integrating these relative flight configurations into a geocentric reference frame, enabling the calculation of the specular point on the Earth's surface.

Once the mechanical challenges had been identified, different formations were designed based on physical principles. To compare these flight formations, an initial analysis based on array factors was carried out. This analysis directly eliminated configurations that did not meet electromagnetic requirements, consisting of a beamwidth of 1 km and sidelobes below -10 dB within the glistening zone.

After identifying the most promising formations during the initial analysis, a deeper examination was necessary to evaluate how the various orbital constraints influenced ground signal illumination for these configurations. Several tests were conducted to examine the effects of different factors, such as the number of satellites in a constant-radius configuration, the inclination of the Cubesats' plane, the positioning of the GNSS satellite, and the evolution of formations over an orbital period.

In conclusion, flight formations utilizing concentric relative orbits to replicate a spiral shape appear to be the most promising within the scope of this project. While the Y-shaped formation provides satisfactory results in terms of resolution, its drawback lies in its inconsistency over an orbital period. The spiral formations, particularly the 29-satellitse spiral with four equally spaced arms, exhibit greater temporal stability due to their elliptical shape. Concerning the constraint of satellite plane inclination relative to the Earth's surface, the capacity to maintain satisfactory resolution despite this constraint was demonstrated. In fact, the inclination of the satellite plane can even be leveraged to balance the effect of GNSS satellite positioning within the Cubesat formation's horizon. Furthermore, it has been demonstrated that the GNSS satellite exhibits a significant range of permissible displacements with respect to the Cubesats' horizon while maintaining an isotropic resolution. A final relevant finding emerged from the analysis of ground spots. It has been demonstrated that for any position along the orbital period, the constraint associated with the non-static nature of spiral configurations over time can be offset by a suitable tilt of the satellite plane.

Henceforth, the constraints encountered in this project appear ultimately surmountable through a precise selection of the eight initial conditions that govern relative orbital motion. The spiral configuration yielded highly promising outcomes, thereby opening up new horizons and challenges for future research in the field of Earth observation employing formations of Cubesats.

Bibliography

[1] BCcampus. *The Law of Reflection.* URL: `https://tinyurl.com/yckck3y6` (visited on 07/20/2023).

[2] Trevor Bennett and Hanspeter Schaub. “Space-to-space based relative motion estimation using linearized relative orbit elements”. In: *Maui, HI, September* (2015), pp. 15–18.

[3] Encyclopedia Britannica. *Vernal Equinox.* URL: `https://www.britannica.com/science/vernal-equinox` (visited on 07/12/2023).

[4] WH Clohessy and RS Wiltshire. “Terminal guidance system for satellite rendezvous”. In: *Journal of the aerospace sciences* 27.9 (1960), pp. 653–658.

[5] J Kirk Cochran, Henry J Bokuniewicz, and Patricia L Yager. *Encyclopedia of ocean sciences.* Academic Press, 2019.

[6] Christophe Craeye. *Antennas and Propagation.* Lecture Notes. Chapter 2. Université catholique de Louvain (UCL), 2023. (Visited on 03/26/2023).

[7] Simone D’Amico. “Autonomous formation flying in low earth orbit”. PhD thesis. TU Delft, 2010.

[8] Peter Delos, Bob Broughton, and Jon Kraft. “Phased array antenna patterns-part 1: Linear array beam characteristics and array factor”. In: *Analog Dialogue* 54.2 (2020), pp. 1–8.

[9] H Djojodihardjo. “Influence of the earth’s dominant oblateness parameter on the low formation orbits of micro-satellites”. In: *International Journal of Automotive and Mechanical Engineering* 9 (2014), pp. 1802–1819.

[10] Ugo-Paul Duraffourd. “CubeSats in formation for Earth observation”. Preliminary work on Earth shape modeling. 2021-2022.

[11] ESA. *Galileo Navigation Signals and Frequencies.* URL: `https://www.esa.int/Applications/Navigation/Galileo/Galileo_navigation_signals_and_frequencies` (visited on 06/10/2023).

[12] ESA. *Galileo satellites.* URL: `https://www.esa.int/Applications/Navigation/Galileo/Galileo_satellites` (visited on 05/31/2023).

[13] European Union Agency for the Space Programme (EUSPA). *What is GNSS?* 2021. URL: `https://www.euspa.europa.eu/european-space/eu-space-programme/what-gnss` (visited on 06/13/2023).

[14] ANSYS Learning Hub. *Argument of Perigee.*

[15] ANSYS Learning Hub. *Right Ascension of the Ascending Node.*

[16] Sean Victor Hum. "Lorentz Reciprocity Theorem". In: ().

[17] D Ivanov, M Kushniruk, and M Ovchinnikov. "Study of satellite formation flying control using differential lift and drag". In: *Acta Astronautica* 152 (2018), pp. 88–100.

[18] Per-Simon Kildal. *Foundations of antenna engineering: a unified approach for line-of-sight and multipath.* Artech House, 2015.

[19] Wei Liu and Stephan Weiss. *Wideband beamforming: concepts and techniques.* John Wiley & Sons, 2010.

[20] Javier Martín and Simone Centuori. "Quasi-Satellite Orbits around Phobos for the Sample Return Mission". In: ().

[21] Mathuranathan. *Array Pattern Multiplication of Phased Array Antennas.* 2021. URL: `https://www.gaussianwaves.com/2021/11/array-pattern-multiplication-of-phased-array-antennas/` (visited on 04/09/2023).

[22] Mathuranathan. *Far-field retarded potentials.* 2021. URL: `https://www.gaussianwaves.com/2021/11/far-field-retarded-potentials/` (visited on 04/09/2023).

[23] NASA. *CubeSat 101: Basic Concepts and Processes for First-Time CubeSat Developers.* NASA. 2018. URL: `https://www.nasa.gov/sites/default/files/atoms/files/nasa_csli_cubesat_101_508.pdf` (visited on 03/26/2023).

[24] Sophocles J. Orfanidis. *Electromagnetic Waves and Antennas.* 2008. URL: `http://eceweb1.rutgers.edu/~orfanidi/ewa/ch22.pdf` (visited on 04/20/2023).

[25] Eric Reinthal. *Relative Orbit Propagation and Control for Satellite Formation Flying using Continuous Low-thrust.* 2017.

[26] F Scala et al. "Analysis and design of future multiple satellite formation flying L-band missions in low Earth orbit". In: *INTERNATIONAL ASTRONAUTICAL CONGRESS: IAC PROCEEDINGS.* International Astronautical Federation, IAF. 2022, pp. 1–12.

[27] Hanspeter Schaub. "Spacecraft relative orbit geometry description through orbit element differences". In: *14th US National Congress of Theoretical and Applied Mechanics, Blacksburg, VA.* 2002.

[28] SciPy Contributors. *SciPy.optimize.minimize*. SciPy documentation. 2023. URL: `https://docs.scipy.org/doc/scipy/reference/generated/scipy.optimize.minimize.html` (visited on 05/30/2023).

[29] Valentin Sokolow et al. "Scanning GNSS-R Beams from Cubesats Using Sequentially Rotated Deployable Dipoles". In: *2021 IEEE International Geoscience and Remote Sensing Symposium (IGARSS)*. 2021, pp. 8538–8541.

[30] UCAR COSMIC Program. *Global Navigation Satellite System (GNSS) Reflectometry Background*. 2023. URL: `https://www.cosmic.ucar.edu/global-navigation-satellite-system-gnss-background/gnss-reflectometry` (visited on 06/28/2023).

[31] Sokolow Valentin et al. "Scanning GNSS-R Beams from Cubesats Using Sequentially Rotated Deployable Dipoles". In: *2021 IEEE International Geoscience and Remote Sensing Symposium IGARSS*. IEEE. 2021, pp. 8538–8541.

[32] David A Vallado. *Fundamentals of astrodynamics and applications*. Vol. 12. Springer Science & Business Media, 2001.

[33] David A Vallado and Salvatore Alfano. "Curvilinear coordinates for covariance and relative motion operations". In: *2011 AAS/AIAA Astrodynamics Specialist Conference*. 2011.

[34] *Very Large Array (VLA) Radio Telescope*. National Radio Astronomy Observatory (NRAO). URL: `https://public.nrao.edu/telescopes/vla/` (visited on 07/28/2023).

[35] Wikipedia. *Satellite Navigation*. URL: `https://en.wikipedia.org/w/index.php?title=Satellite_navigation&oldid=1153673021` (visited on 06/10/2023).

[36] Wikipedia contributors. *Array Factor*. 2023. URL: `https://en.wikipedia.org/wiki/Array_factor` (visited on 04/09/2023).

[37] Wikipedia contributors. *Spherical coordinate system*. 2023. URL: `https://en.wikipedia.org/wiki/Spherical_coordinate_system` (visited on 04/09/2023).

[38] Qingyun Yan, Weimin Huang, and Giuseppe Foti. "Quantification of the relationship between sea surface roughness and the size of the glistening zone for GNSS-R". In: *IEEE geoscience and remote sensing letters* 15.2 (2017), pp. 237–241.

[39] Jesús Peláez Álvarez. *Astrodinámica y Dinámica de Actitud*. Master Universitario en Ingeniería Aeronautica. 2016.

Appendix A

Derivation of the CW equations

The following proof was carried out by Professor Jesús Peláez Álvarez as part of the course "Astrodinámica y Dinámica de Actitud" taught at the Universidad Politécnica de Madrid [39].

A.1 Gravity gradient

Consider a satellite in circular orbit of radius R around the Earth. We aim to analyze the relative motion of a material particle M with mass m evolving in its vicinity with respect to the satellite. For simplicity, we assume the Earth is spherical, such that its gravitational attraction on particle M, located at a distance d from its center, is $m\mu/d^2$ ($\mu = GM_T$, where G is the universal gravitational constant and M_T is the mass of the Earth). Additionally, we neglect any other forces acting on the particle (aerodynamic resistance, solar radiation pressure, etc.).

The center of mass of the satellite is taken as the origin O of a right-handed trirectangular reference system, $Oxyz$, known as the orbital frame. In this frame, the Ox axis coincides with the local vertical ascending direction, the Oz axis aligns with the tangent to the trajectory with its positive direction in the direction of advancement, and the Oy axis is normal to the orbital plane [1]. Since the satellite follows a circular path, the reference frame $Oxyz$ has a constant angular velocity $\vec{\omega} = -\omega\vec{\mathbf{j}}$, given by $\omega = 2\pi/T = \sqrt{\mu/R^3}$ (third law of Kepler).

The vector $\vec{\mathbf{r}} = \vec{\mathbf{OM}} = x\vec{\mathbf{i}} + y\vec{\mathbf{j}} + z\vec{\mathbf{k}}$ represents the position of point M in the orbital reference frame. Its motion, relative to the reference frame Oxyz, is

---

[1] The proof employs a relative coordinate system where the y and z axes do not follow the same conventions as those used in the development of this project.

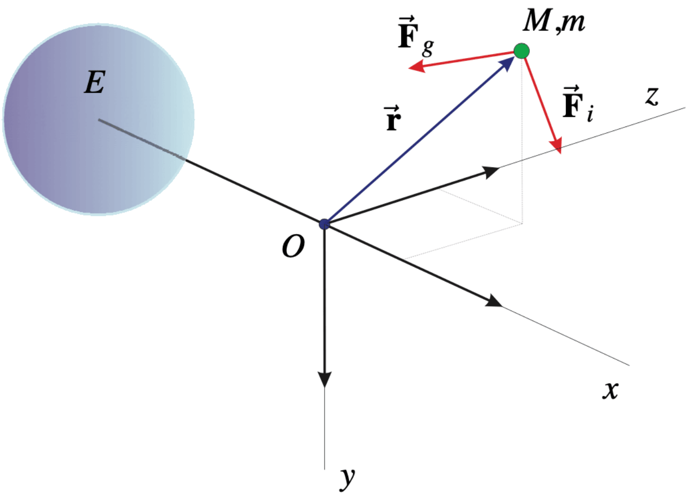

Figure A.1: Relative motion

governed by the following forces:

- **Gravitational attraction**:

$$\overrightarrow{\mathbf{F}}_g = -\left(m\mu/\zeta^3\right)\vec{\zeta}, \quad \vec{\zeta} = \overrightarrow{\mathbf{EM}}$$

(Here, E is the center of mass of the Earth.)

- **Centrifugal force**:

$$\overrightarrow{\mathbf{F}}_{IA} = m\omega^2 R\left(1 + \frac{x}{R}, 0, \frac{z}{R}\right)$$

- **Coriolis inertial force**:

$$\overrightarrow{\mathbf{F}}_{IC} = 2m\omega(\dot{z}, 0, -\dot{x}).$$

Here, $\vec{\mathbf{v}} = (\dot{x}, \dot{y}, \dot{z})$ is the velocity of the particle; note that the component of the inertia forces on the Oy axis, normal to the orbit, is null.

If the position vector of particle M with respect to Earth is written as:

$$\vec{\boldsymbol{\zeta}} = \overrightarrow{\mathbf{EM}} = R\vec{\mathbf{i}} + \vec{\mathbf{r}}$$

the gravitational force, $\vec{\mathbf{F}}_g$ becomes:

$$\vec{\mathbf{F}}_g = -m\omega^2 R\left[\vec{\mathbf{i}} + \frac{1}{R}(-2x\vec{\mathbf{i}} + y\vec{\mathbf{j}} + z\vec{\mathbf{k}}) - \frac{3}{2R^2}((2x^2 - y^2 - z^2)\vec{\mathbf{i}} - 2xy\vec{\mathbf{j}} - 2xz\vec{\mathbf{k}}) + o(\varepsilon^2)\right]$$

where the dimensionless number $\varepsilon_1 = |\vec{\mathbf{r}}|/R$ is small, as we assume the particle M is located in the vicinity of the satellite O. If terms of order $O(\varepsilon^2)$ or higher are neglected, we obtain the following approximate expression for $\vec{\mathbf{F}}_g$:

$$\vec{\mathbf{F}}_g \approx -m\omega^2 R\left[\vec{\mathbf{i}} + \frac{1}{R}(-2x\vec{\mathbf{i}} + y\vec{\mathbf{j}} + z\vec{\mathbf{k}})\right]$$

Gravity and centrifugal force

$$\overrightarrow{\mathbf{F}}_{IA} = m\omega^2 R\left\{\overrightarrow{\mathbf{i}} + \frac{1}{R}(x\,\overrightarrow{\mathbf{i}} + z\,\overrightarrow{\mathbf{k}})\right\}$$

are composed of terms of different orders of magnitude. In both forces, the unit order terms are equal and of opposite signs. Their resultant, $\overrightarrow{\mathbf{F}}_{gg}$:

$$\overrightarrow{\mathbf{F}}_{gg} = \overrightarrow{\mathbf{F}}_g + \overrightarrow{\mathbf{F}}_{IA}$$

is called the gravity gradient and does not contain terms of order unity because they cancel. The terms of order $O\left(\varepsilon_1\right)$, which constitute the most important part of the force itself, take the form:

$$\overrightarrow{\mathbf{F}}_{gg} \approx m\omega^2(3x\,\overrightarrow{\mathbf{i}} - y\,\overrightarrow{\mathbf{j}})$$

and cancel at the origin, where the gravitational force is exactly offset by the centrifugal force. The gravity gradient is composed of the term $3m\omega^2 x\vec{\mathbf{i}}$, a repulsion from the horizontal plane Oyz proportional to mass and distance, and the term $-m\omega^2 y\vec{\mathbf{j}}$, an attraction from the orbital plane Oxz proportional to mass and distance. To obtain the resultant of the forces acting on M, the Coriolis inertial force must be added to the gravity gradient. Consequently, the acceleration acting on particle M is:

$$\overrightarrow{\mathbf{f}} \simeq \omega^2(3x\,\overrightarrow{\mathbf{i}} - y\,\overrightarrow{\mathbf{j}}) + 2\omega(\dot{z}\,\overrightarrow{\mathbf{i}} - \dot{x}\,\overrightarrow{\mathbf{k}})$$

For a particle located in the local vertical and at rest, the acceleration acting on each of its particles reduces to:

$$\overrightarrow{\mathbf{f}} \simeq 3\omega^2 x\,\overrightarrow{\mathbf{i}}$$

A.2 Clohessy-Wiltshire equations

Obviously, the gravitational force $\overrightarrow{\mathbf{F}}_g$ is a conservative force derived from the ordinary gravitational potential V_1.

$$V_1 = -\frac{m\mu}{\zeta} = -\frac{m\mu}{R\sqrt{1 + 2\frac{\overrightarrow{\mathbf{r}}\cdot\overrightarrow{\mathbf{i}}}{R} + \frac{\overrightarrow{\mathbf{r}}^2}{R^2}}}.$$

After neglecting terms of higher order than ε_1^2, the potential V_1 takes on the form

$$V_1 = \frac{m\mu}{R}\left(\frac{\overrightarrow{\mathbf{r}}\cdot\overrightarrow{\mathbf{i}}}{R} - \left\{\frac{3}{2}\left(\frac{\overrightarrow{\mathbf{r}}\cdot\overrightarrow{\mathbf{i}}}{R}\right)^2 - \frac{1}{2}\frac{\overrightarrow{\mathbf{r}}^2}{R^2}\right\} + o\left(\varepsilon_1^2\right)\right)$$

On the other hand, the inertial drag and Coriolis forces derive from the following generalized potential

$$V_2 = \frac{1}{2}m\left(2\vec{\gamma}_{01}^O\cdot\overrightarrow{\mathbf{r}} - \left(\vec{\omega}_{01}\times\overrightarrow{\mathbf{r}}\right)^2\right) - m\vec{\omega}_{01}\cdot\left(\overrightarrow{\mathbf{r}}\times\dot{\overrightarrow{\mathbf{r}}}\right)$$

where $\vec{\omega}_{01}$ is the angular velocity of the orbital frame and $\vec{\gamma}_{01}^O$ is the acceleration of its origin with respect to the inertial geocentric reference. Both are given by

$$\vec{\omega}_{01} = -\omega\,\overrightarrow{\mathbf{j}}, \quad \vec{\gamma}_{01}^O = -\omega^2 R\,\overrightarrow{\mathbf{i}}$$

In terms of the coordinates and their derivatives, the potentials V_1 and V_2 turn out to be:

$$V_1 = m\omega^2\left\{Rx + \frac{1}{2}\left(-2x^2 + y^2 + z^2\right)\right\}$$
$$V_2 = m\omega^2\left\{-Rx - \frac{1}{2}\left(x^2 + z^2\right)\right\} + m\omega(z\dot{x} - \dot{z}x)$$

Thus, the generalized potential $V = V_1 + V_2$ from which all the forces acting on the particle derive will be:

$$V = \frac{1}{2}m\omega^2\left\{-3x^2 + y^2\right\} + m\omega(z\dot{x} - \dot{z}x)$$

In terms of the potential V, the components of the force acting on the particle can be expressed as follows:

$$f_x = -\frac{\partial V}{\partial x} + \frac{\mathrm{d}}{\mathrm{d}t}\left(\frac{\partial V}{\partial \dot{x}}\right) = m\left(3\omega^2 x + 2\omega\dot{z}\right)$$
$$f_y = -\frac{\partial V}{\partial y} + \frac{\mathrm{d}}{\mathrm{d}t}\left(\frac{\partial V}{\partial \dot{y}}\right) = -m\omega^2 y$$
$$f_z = -\frac{\partial V}{\partial z} + \frac{\mathrm{d}}{\mathrm{d}t}\left(\frac{\partial V}{\partial \dot{z}}\right) = -2m\omega\dot{x}$$

Since only quadratic terms have been retained in the gravitational potential, the forces depicted are merely an approximation and lead to linear equations governing, in the first approximation, the relative motion of M with respect to the satellite.

The equations governing the motion of M are:

$$\begin{aligned}
\ddot{x} &= 3\omega^2 x + 2\omega \dot{z} \\
\ddot{y} &= -\omega^2 y \\
\ddot{z} &= -2\omega \dot{x}
\end{aligned}$$

UNIVERSITÉ CATHOLIQUE DE LOUVAIN
École polytechnique de Louvain
Rue Archimède, 1 bte L6.11.01, 1348 Louvain-la-Neuve, Belgique | **www.uclouvain.be/epl**